



A combined rate theory-population balance model of the evolution of irradiation-induced helium bubbles in metals during annealing

Qi Li, Chibin Zhang, XiaoHui Lin, Chenlong Liu, Yan Xing*

Jiangsu Key Laboratory for Design and Manufacture of Micro-Nano Biomedical Instruments, Department of Mechanical Engineering, Southeast University, Nanjing 211189, China



ARTICLE INFO

Article history:

Received 2 May 2022

Revised 4 November 2022

Accepted 4 November 2022

Available online 6 November 2022

Keywords:

Irradiation

Helium bubble evolution

Population balance equation

Rate equations

ABSTRACT

A multiscale model describing the evolution of helium bubbles in the irradiated materials is established based on the rate equations and the population balance equation. The size distribution of the helium bubbles and the evolution law of the statistical average size and number density of the bubbles with time changing predicted by the model are in good agreement with the experimental statistics. The influence of annealing temperature, annealing time, irradiation energy, irradiation flux, and coarsening mechanisms on the evolution of helium bubbles are numerically simulated and discussed, taking FeCrAl alloy as the irradiated material. The results show that the bubble evolution is dominated by the Ostwald ripening mechanism under high temperature annealing conditions (≥ 1073 K), and the time dependence of the average size and density of helium bubbles is consistent with the existing theoretical results. And the number of shrinking helium bubbles caused by Ostwald ripening is effectively reduced by the bubble coalescence effect, leading to further growth of the proportion of large-sized helium bubbles. Consequently, a Gaussian bubble size distribution has been obtained modeling the coupling of the Ostwald ripening mechanism and the bubble coalescence mechanism. The generation rates of helium and vacancy in the material during irradiation, as well as their ratio, are significant factors that can affect the nucleation and evolution of helium bubbles.

© 2022 Elsevier B.V. All rights reserved.

1. Introduction

Irradiation can produce defects in materials, which modify the mechanical and electromagnetic properties of the materials [1,2]. In most cases, the irradiation defect is an unavoidable negative product that would impair the properties of the materials, and the most typical case is the structural components of nuclear reactors which are exposed to high levels of radiation [3,4]. In the irradiation environment, high-energy particles collide with atoms in the material lattice, creating vacancies and interstitial atoms [5,6], while insoluble helium produced by D-T fusion reactions as well as the (n, α) transmutation reactions [7] tends to migrate rapidly and quickly and combine with vacancies to form helium-vacancy clusters [8]. Helium-vacancy clusters eventually precipitate nanoscale helium bubbles in the structural components of the nuclear reactor [9] as a result of thermal effects and cascade collisions, and these helium bubbles then undergo a complex dynamic evolution as the average size of the bubbles grows [10]. The performance of structural materials of nuclear reactors will be considerably weak-

ened by the enormous helium bubbles, eventually leading to catastrophic failure [11–13]. Furthermore, as nanotechnology has advanced, the focused helium ion beams have been used to create nanoscale features [14] and to perform high-resolution imaging [15], which also inevitably causes helium irradiation damage to the substrate material [16]. Consequently, modeling the formation and evolution of helium bubbles, as well as investigating the mechanisms involved, is critical for assessing the irradiation properties and improving the service performance of irradiated structural materials of nuclear reactors, and furthering the development of irradiation damage theory.

Over the last few decades, many efforts have been made in computer simulation to simulate and reveal the generation and evolution of helium bubbles [17]. However, it is a complex cross-scale process from the generation of defects to the evolution of nanoscale helium bubbles. Therefore, it is almost unfeasible to complete the simulation with a single simulation model, and a multi-scale coupling model must be applied. The initial crystal defect distribution generated in picosecond time from the incident high-energy particle to the substrate can be calculated using the binary collision approximation (BCA) and the widely used SRIM program [18] is a prominent BCA example. After obtaining the initial distribution of defects and gathering the migration proper-

* Corresponding author.

E-mail address: xingyan@seu.edu.cn (Y. Xing).

Nomenclature	
B	van der Waals constant (dimensionless)
b	re-solution parameter (dimensionless)
C_s^v	equivalent dispersed vacancy sink concentration (dimensionless)
C_s^i	equivalent dispersed self-interstitials sink concentration (dimensionless)
D_i	diffusion coefficients of self-interstitials (m^2/s)
D_g	diffusion coefficients of helium (m^2/s)
D_v	diffusion coefficients of vacancies (m^2/s)
e_1	thermal emission probability from substitutional helium (dimensionless)
e_2	thermal emission probability from a vacancy-di-helium cluster (dimensionless)
e_3	dissociation probability for a di-gas atom cluster (dimensionless)
k_i	frequency factor for recombination (1/s)
k_g	frequency factor for helium (1/s)
k_v	frequency factor for vacancies (1/s)
k_{rs}	re-solution frequency (1/s)
K_B	Boltzmann's Constant (J/K)
n_a	number density of material atoms ($1/\text{m}^3$)
s_f	fraction of vacancies surviving cascade instantaneous recombination (dimensionless)
t_{irr}	irradiation time (s)
T	temperature (K)
T_m	absolute melting point (K)
γ_b	surface tension (N/m)
ε	diffusion-control combinatorial factor for bubbles (dimensionless)
ζ	projection of helium bubble motion direction vector in the x -axis direction (dimensionless)
κ	projection of helium bubble motion direction vector in the z -axis direction (dimensionless)
ρ	dislocation density (m/m^3)
ω_i	bias factor for self-interstitials (dimensionless)
ω_v	bias factor for vacancies (dimensionless)
Ω	atomic volume ($1/\text{m}^3$)

ties of all relevant defects, the diffusion and nucleation of defects could be modeled using the kinetic Monte Carlo (KMC) [19] or reaction rate equations (RE) method [20,21]. The KMC method is a general way to simulate the time evolution of any system with known rates by probabilistically selecting the transition, provided the subsequent transitions are not correlated with each other and are Poisson processes. The rate equations are continuous differential equations about the density of defects, and the diffusion and nucleation of defects could be simulated by solving these equations. Both approaches have their advantages; the computational efficiency of RE is higher for models with low spatial dimensions, and the calculation results of the KMC method are more accurate when all input parameters are correct. The next stage of the simulation is the further evolution of the helium bubbles at the nanoscale, and the simulation methods at this stage are mostly based on the object kinetic Monte Carlo (OKMC) method [22–24] and the molecular dynamics (MD) method [25,26]. The Object kinetic Monte Carlo method has proven to be an effective tool to understand microstructure evolution, and the molecular dynamics method is more commonly employed to investigate the effects of mechanisms and parameters on an individual helium bubble. However, there are still some limitations in the existing methods for simulating the evolution of helium bubbles. The enlargement of the helium bubble population directly increases the computa-

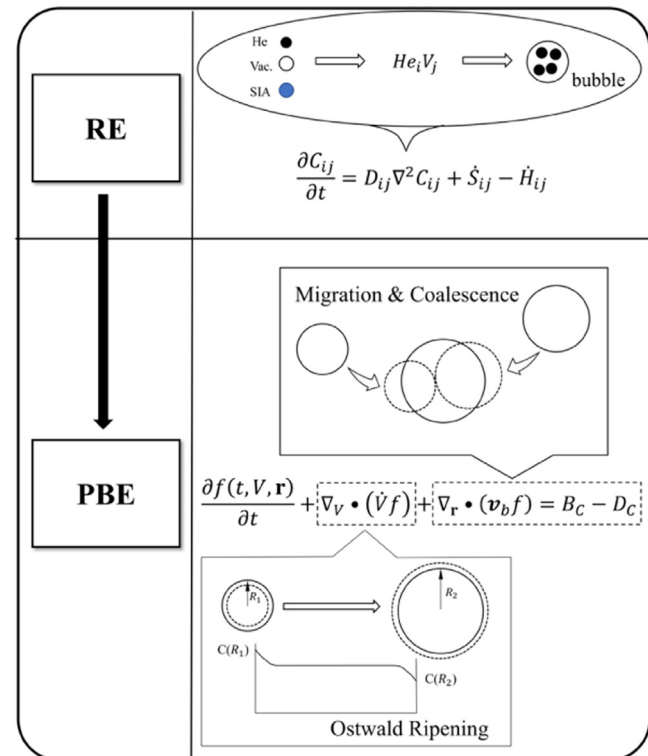


Fig. 1. Overview of the combined model in this paper and its simulation objects.

tional time of OKMC, and the MD method is powerless to simulate the dynamics of the system for a long period. Two widely recognized mechanisms in the evolution of nanoscale helium bubbles are the “Migration and coalescence (MC)” and “Ostwald ripening (OR)” [27]. Additionally, the continuous growth of helium bubbles through the absorption of point defects is not negligible at insufficiently high temperatures. Although there have been successful efforts to simulate the helium bubble coalescence using OKMC, it is difficult to reasonably give the probabilities of Ostwald ripening and continuous growth processes in the evolution of helium bubbles. Moreover, the simulation accuracy and efficiency of OKMC rely on empirical value excessively, which leads to magnified limitations when considering the coupling effect of multiple mechanisms, thus the analysis of coupling effects between mechanisms would be affected.

The population balance equation (PBE) is a physical statement to describe the population evolution of countable entities based on the theory of continuum media mechanics [28]. The equation contains both continuous changes due to continuous molecular and atomic processes and discontinuous changes due to discrete events in elemental properties of interest, which match up with the processes involved in the evolution of helium bubbles. To overcome the s of the OKMC and MD methods in simulating bubble evolution and to simulate the evolution of helium bubbles under thermal conditions quantitatively, a combined model consisting of a helium bubble nucleation model dominated by rate equations and a helium bubble population evolution model based on the population balance equation is developed in this research. An overview of the present combined model and its simulation objects is shown in Fig. 1. The calculated results of rate equations will be used as the initial condition for the population balance equation. The migration, coalescence, absorption of point defects and Ostwald ripening mechanisms during the evolution of helium bubbles have corresponding description terms in the helium bubble population balance equation established in this paper with respective numeri-

cal solutions. The reactions between three kinds of point defects, four kinds of composite defects and helium bubble nuclei are described in the rate equations in this paper, and RE is chosen as the simulation method for the helium bubble nucleation because its computational efficiency is independent of the size of the helium bubble population being simulated. The calculated results of the model in this paper will be compared with the statistical results of helium bubbles inside the irradiated Molybdenum (Mo) and FeCrAl with a normal chemical composition of Fe-13.2Cr-5.6Al-2Mo-2ZrC (wt.%) obtained by Transmission Electron Microscopy (TEM) in Refs. [29,30] to verify the reliability of the model. Mo is a promising candidate material for innovative nuclear power systems with high temperature strength, high melting point, and good thermal conductivity [31]. FeCrAl alloy is regarded as an excellent potential candidate for accident tolerant fuel claddings used in commercial light water reactors (LWRs) due to its good high-temperature oxidation resistance [32], mechanical properties, and irradiation resistance. Thus, irradiation properties are the key factors to assess the service performance of Mo and FeCrAl alloys. The effects of annealing temperature and time, irradiation energy and dose on the evolution of helium bubbles are simulated and analyzed in this paper using the coupling model, and the key mechanisms and factors affecting the evolution are discussed and summarized. There are unique phason defects that are likely to exist in some special alloys containing icosahedral quasicrystals [33,34], which dominate a unique atomic jumping mechanism with very low activation energy. However, the phason mechanism is neglected in the experiments and simulations involved in the current work because of its high dependence on sufficiently low temperatures [35].

The paper is organized as follows. In Section 2, we present details of the theoretical development of the coupling model, and the procedures of its numerical solution are presented in Section 3. Then the verification and results are presented in Section 4 with discussions of the key mechanisms and factors that play a role in the evolution of helium bubbles. Finally, conclusions are given in Section 5.

2. Theoretical model

In the following, we describe the present multiscale coupling model in the order of the helium bubble evolution timeline. The SRIM-2010 program [18] is applied to compute the required helium implantation depth and vacancy implantation rate for nucleation calculations with specific ion energy and angle of incidence. A system of rate equations is established for modeling the nucleation and early growth of bubbles. This is followed by a helium bubble population balance equation developed to treat the processes of motion, coalescence and Ostwald ripening of nucleated bubbles. The following assumptions are made to simplify the modeling framework:

- (1) Only point defects are absorbed by the helium bubble, compound defects do not interact with the helium bubbles.
- (2) The coalescence of helium bubbles always satisfies only volume conservation and does not change to surface area conservation with time and temperature.

2.1. The rate equations for the nucleation of helium bubbles

The evolution of helium bubbles in the irradiated material can normally be divided into two stages, the first stage is called the nucleation of helium bubbles. Vacancies, self-interstitial atoms and deposited helium ions are continuously generated in the substrate material due to the irradiation of the helium ion beam. The critical helium nucleus and helium bubbles are formed due to the diffusion of point defects and the reactions between various defects,

and the concentration evolution of various types of defects and helium bubbles in the nucleation stage could be described by the rate equations, and the rate equations for the concentration of α -type and β -type defects could be written as [21,36]:

$$\frac{\partial C_\alpha}{\partial t} = D_\alpha \nabla_r^2 C_\alpha + \dot{S}_\alpha - \dot{H}_\alpha, \quad (1-a)$$

$$\frac{\partial C_\beta}{\partial t} = \dot{S}_\beta - \dot{H}_\beta, \quad (1-b)$$

the α -type defects in Eq. (1-A) include self-interstitial atoms (SIA) (i), vacancies (v) and helium interstitials (g), while the β -type defects in Eq. (1-B) represent the composite defects generated by the interaction of α -type defects and include helium substitutional atoms (gv), di-helium interstitials ($2g$), di-helium mono-vacancy ($2gv$) and the critical nucleus (cn).

The critical nucleus size is a cluster of 3 gas atoms and some vacancies (need not be exactly determined). The combinations that can form a stable nucleus in this paper are $2gv + g \rightarrow 3gv$ and $2g + g \rightarrow 3g$. The reason why it is called 'critical' nucleus is that a critical nucleus transformed into a helium bubble recognized in our model when absorbing a vacancy or helium atom

The first term on the right side of Eq. (1-A) is the diffusive flux of the α -type defects in the spatial dimension (r), and the second term and the third term on the right side of Eq. (1-A) are the source and sink expressions of the α -type defects, respectively. Similarly, the two terms on the right side of Eq. (1-B) are the source and sink expressions of the β -type defects, respectively.

The source and sink expressions of the α -type defects are written as [21,36]:

$$\dot{S}_i = s_f G_{FP}$$

$$\dot{H}_i = k_i C_i (C_v + C_{gv} + 2C_{2gv} + 3C_{cn} + C_s^i),$$

$$\dot{S}_v = s_f G_{FP} + (k_g e_1 + k_{rs}) C_{gv}$$

$$\dot{H}_v = C_v [k_i C_i + k_g C_g + k_v (C_{gv} + 2C_{2gv} + 2C_{2g} + 3C_{cn} + C_s^v)]$$

$$\dot{S}_g = G_{He} + k_g (e_1 C_{gv} + 2e_3 C_{2g} + e_2 C_{2gv})$$

$$+ k_{rs} (C_{gv} + 2C_{2gv} + 2(2C_{2g}) + 3C_{cn} + n_{He} C_b) + k_i C_i (C_{gv} + 3C_{cn})$$

$$\dot{H}_g = k_g C_g (C_v + C_{gv} + 4C_g + 2C_{2gv} + 2C_{2g} + 3C_{cn} + \varepsilon C_b)$$

and the source and sink expressions of the β -type defects are written as [21,36]:

$$\dot{S}_{gv} = k_g e_2 C_{2gv} + 2k_{rs} C_{2gv} + k_g C_g C_v + 2k_v C_v C_{2gv},$$

$$\dot{H}_{gv} = C_{gv} (k_g e_1 + k_{rs} + k_i C_i + k_g C_v)$$

$$\dot{S}_{2g} = 2k_i C_i C_{2gv} + 2k_g C_g^2$$

$$\dot{H}_{2g} = C_{2g} (k_g e_3 + 2k_{rs} + 2k_v C_v + 2k_g C_g),$$

$$\dot{S}_{2gv} = 3k_{rs} C_{cn} + k_g C_g C_{gv} + 2k_v C_v C_{2g}$$

$$\dot{H}_{2gv} = C_{2gv} (k_g e_2 + 2k_{rs} + 2k_i C_i + 2(k_g + k_v) C_v),$$

$$\dot{S}_{cn} = 2k_g C_g (C_{2gv} + C_{2g})$$

$$\dot{H}_{cn} = 3C_{cn} (k_{rs} + k_i C_i + k_g C_g + k_v C_v).$$

The initial conditions of Eqs. (1-A) and (1-b) are $C_i(\mathbf{r})|_{t=0} = C_{i0}$, $C_v(\mathbf{r})|_{t=0} = C_{v0}$, $C_g(\mathbf{r})|_{t=0} = 0$, $C_\beta(\mathbf{r})|_{t=0} = 0$, where, $C_{i0} = \exp(-\frac{E_f}{k_B T})$ and $C_{v0} = \exp(-\frac{E_v}{k_B T})$ are the concentrations of the thermal equilibrium interstitials and vacancies.

The rate equations for the concentration of helium bubbles (C_b), the average number of helium atoms in a bubble (n_{He}) and the average radius of the helium bubbles (R_b) could be written as [21,36]:

$$\frac{\partial C_b}{\partial t} = \frac{1}{n_{He}} (12k_g C_g C_{cn} + 9k_v C_v C_{cn}), \quad (2-a)$$

$$\frac{\partial n_{He}}{\partial t} = \varepsilon k_g C_g - k_{rs} n_{He}, \quad (2-b)$$

$$\frac{\partial R_b}{\partial t} = \frac{1}{R_b} \left\{ D_v C_v - D_i C_i + D_v C_{v0} \left[\frac{\Omega}{K_B T} \left(P - \frac{2\gamma_b}{R_b} \right) - 1 \right] \right\}, \quad (2-c)$$

where, $P = n_{He} K_B T / (\frac{4}{3}\pi R_b^3 - n_{He} B)$ is the internal gas pressure. And the surface tension γ_b is fitted to a linear temperature dependence $\gamma_b = 3.77 - 4.35 \times 10^{-4} T$ [21,37].

The initial conditions of Eqs. (2-a), (2-b) and (2-c) are $C_b(\mathbf{r})|_{t=0} = 0$, $n_{He}(\mathbf{r})|_{t=0} = 3$, $R_b(\mathbf{r})|_{t=0} = 0.3$ nm.

All concentrations involved in the rate equations in this paper are dimensionless by multiplying by an atomic volume (Ω), e.g. C_i (dimensionless) = $C_i(1/m^3) \times \Omega$.

There are many parameters and symbols in the rate equations above, and the key parameters are next categorically defined with reference to Ref. [36]. The reaction frequency of self-interstitials (k_i), helium (k_g) and vacancies (k_v) and re-solution frequency (k_{rs}) are $k_i = 48\nu_i \exp(-E_m^i/(K_B T))$, $k_g = 48\nu_g \exp(-E_m^{He}/(K_B T))$, $k_v = 48\nu_v \exp(-E_m^v/(K_B T))$, and $k_{rs} = bG_{FP}$. The diffusion coefficients of self-interstitial, vacancy, and helium interstitial are $D_i = a_0^2 \nu_i \exp(-E_m^i/(K_B T))$, $D_g = a_0^2 \nu_g \exp(-E_m^{He}/(K_B T))$, and $D_v = a_0^2 \nu_v \exp(-E_m^v/(K_B T))$, and the diffusion-control combinational factor of helium bubbles $\varepsilon = 4\pi/48(R_b/a_0)$. The basic thermal emission probabilities are $e_1 = \exp(-E_b^{v,g}/(K_B T))$, $e_2 = \exp(-E_b^{v,2g}/(K_B T))$, and $e_3 = \exp(-E_b^{2g}/(K_B T))$. The equivalent dispersed sink concentrations of vacancy and self-interstitial are $C_s^v = (a_0^2/48)(\omega_v \rho + 4\pi R_b C_b/\Omega)$ and $C_s^i = (a_0^2/48)(\omega_i \rho + 4\pi R_b C_b/\Omega)$. The more comprehensive definitions of symbols and material parameters can be found in the Nomenclature section and Table I and Table II.

The space-dependent rate theory utilizes, as input, the results of helium and point defect deposition from SRIM simulations of collision cascades. The generation of helium (G_{He}) and Frenkel Pairs (G_{FP}) can be calculated by the following Eqs. (3-a) and (3-b) [38] after obtaining ion deposition 'Range' and damage events 'Vacancy' from output files of the SRIM program. These conversion formulas use irradiation fluence as a multiplier while the denominator contains the atom density and irradiation time.

$$G_{He}(\text{appm/s}) = \frac{\text{Fluence} \left(\frac{\text{ions}}{\text{cm}^2} \right) \times \overbrace{\text{Range} \left(\frac{\text{atoms/cm}^3}{\text{atoms/cm}} \right)}^{\text{range.txt}}}{n_a(\text{atoms/cm}^3) \times t_{irr}(s)} \times 10^6, \quad (3-a)$$

$$G_{FP}(\text{dpa/s}) = \frac{\text{Fluence} \left(\frac{\text{ions}}{\text{cm}^2} \right) \times 10^8 \left(\frac{\text{\AA}}{\text{nm}} \right) \times \overbrace{\text{Vacancy} \left(\frac{\text{vacancies}}{\text{ions} \times \text{\AA}} \right)}^{\text{vacancy.txt}}}{n_a(\text{atoms/cm}^3) \times t_{irr}(s)}, \quad (3-b)$$

The bubble density distribution and average radius distribution of the helium bubbles at the end of the nucleation stage ($C_b(\mathbf{r}, t = t_{nend})$, $R_b(\mathbf{r}, t = t_{nend})$) which could be stored and used as the initial conditions of the second stage could be determined by numerically solving the set of rate equations mentioned above.

2.2. The population balance equation for the migration and coarsening of helium bubbles

The second stage of the helium bubble evolution is the migration and coarsening stage, in which the size and density distribution of helium bubbles change significantly more than that in the first stage. The two widely recognized mechanisms (MC and OR) that work in this stage along with the growth of the bubble due to absorption of surrounding vacancies could be described by a population balance equation for helium bubbles. The PBE is a continuity statement that governs the evolution of a number density function $f(t, V, \mathbf{r})$, which defines the distribution of the helium bubbles over the internal coordinate at any time instant and physical position. In this paper, it is assumed that the total volume remains constant before and after the helium bubble coalescence, and the helium bubbles are all standard spherical in shape, so the helium bubble volume V is naturally chosen to be the internal coordinate in the population balance equation. A phase space $\Omega_{V \times \mathbf{r}}$ can be constructed by internal coordinate V and space coordinates \mathbf{r} , then the PBE takes the following form (4):

$$\frac{\partial f(t, V, \mathbf{r})}{\partial t} + \nabla_{\mathbf{r}} \bullet (\mathbf{v}_b f) + \nabla_V \bullet (\dot{V} f) = B_C - D_C. \quad (4)$$

The second term on the left side of PBE is the migration term which refers to the change in the spatial location of the helium bubbles due to surface diffusion, the third term on the left side of PBE is the growth term in which \dot{V} is the rate of change of the bubble volume due to continuous processes, and the coalescence term which describes the discontinuous changes in the volume of the bubbles due to coalescence is on the right side of Eq. (4).

Surface diffusion is an important mechanism by which helium bubbles move irregularly in a solid and will typically dominate for sub-micron sizes (less than 1 μm) and temperatures lower than the absolute melting point [39,40]. Surface diffusion is adopted as the mechanism dominating the motion of helium bubbles under the experimental and simulation conditions covered in this paper. The surface atoms are in a constant state of motion on the inner surface of the helium bubble, and the net displacement of a large number of these surface atoms can be expressed as a small displacement of the entire bubble, and when the surface atoms make random motions, the resulting bubble motion is a Brownian motion [41,42]. According to Einstein's formula [43], the mean-square displacement during a sufficiently long time Δt can be expressed as

$$\langle (\Delta r)^2 \rangle = \langle [r(1) - r(0)]^2 \rangle = 4D_b \Delta t, \quad (5)$$

then the mean velocity measured over an interval of time Δt is

$$\overline{v_b} = \frac{\sqrt{\langle [r(1) - r(0)]^2 \rangle}}{\Delta t} = \sqrt{\frac{4D_b}{\Delta t}}, \quad (6)$$

where, $r(1)$ is the end position, $r(0)$ is the initial position, and D_b is the effective bubble diffusion coefficient. The effective bubble diffusion coefficient is determined by the following equation [40]

$$D_b = \frac{3a_0^4 D_s}{2\pi R_b^4}, \quad (7)$$

where, the surface diffusion coefficient $D_s = D_0 \exp(-\frac{E_s}{K_B T})$, $D_0 = a_0^2 \nu_s / 4$ is the pre-exponential where ν_s is the jump frequency of surface atoms, usually assumed to be of the order of 10^{13} s^{-1} [44], and $E_s = 7.5 \times 10^{-4} T_m$ [44] is the surface activation energy. The motion direction of the helium bubble is random and can be determined by random sampling.

The coalescence term includes the coalescence birth term B_C and the coalescence death term D_C , and the physical meaning of B_C is that two bubbles with volumes of ξ and $V - \xi$ merged into a

bubble with a volume of V , and the expression for B_C is written as

$$B_C = \frac{1}{2} \int_0^V c(\xi, V - \xi) f(\xi) f(V - \xi) d\xi. \quad (8)$$

The physical meaning of D_C is that the bubbles with a volume of V coalesce with a bubble of a volume of ξ to become a bubble with a volume greater than V , and the expression for D_C is written as

$$D_C = f(V) \int_0^\infty c(V, \xi) f(\xi) d\xi. \quad (9)$$

The expression of the coalescence kernel function $c(V, \xi)$ applied in this paper is

$$c(V, \xi) = K_1 h_c(V, \xi) \lambda_c(V, \xi), \quad (10)$$

and the kernel function consists of the coalescence rate $h_c(V, \xi)$ and the coalescence efficiency $\lambda_c(V, \xi)$ with the description as follows [45]:

$$h_c(V, \xi) = \frac{\pi}{4} \left[\left(\frac{3}{4\pi} \right)^{1/3} (V^{1/3} + \xi^{1/3}) \right]^2 (\bar{v}_b^2(V) + \bar{v}_b^2(\xi))^{\frac{1}{2}}, \quad (11)$$

and

$$\lambda_c(V, \xi) = \exp \left[-K_2 (R_c(V, \xi))^{\frac{5}{6}} \right], \quad (12)$$

where, K_1, K_2 are empirical coefficients and $R_c(V, \xi) = \frac{1}{2}(V^{-\frac{1}{3}} + \xi^{-\frac{1}{3}})^{-1}$.

The change rate of volume for helium bubbles \dot{V} is constituted by the change rate due to absorption of the point defect and the change rate due to Ostwald ripening. According to the calculation results of the present nucleation model, the implanted helium, vacancies and interstitial atoms have been almost consumed in the nucleation process, so it is mainly the thermal vacancies that are absorbed by helium bubbles during annealing. From Eq. (2-C), the change rate of bubble volume due to absorption of thermal vacancy could be obtained as

$$\dot{V}_{def} = 4\pi \Omega \left(\frac{3V}{4\pi} \right)^{\frac{1}{3}} \left[\frac{\Omega}{K_B T} \left(P - \frac{2\gamma_b}{R_b} \right) D_v C_{v0} \right]. \quad (13)$$

The change rate of bubble volume due to Ostwald ripening employed in our model is based on the form proposed by Dai and Nassar [46]:

$$\dot{V}_{Ost} = \frac{8\pi \gamma_b \Omega}{K_B T} D_v C_{v0} \left(3 \sqrt{\frac{V}{V_b}} - 1 \right), \quad (14)$$

where, $\langle V_b \rangle$ is the critical volume which is equivalent to the average volume and can be calculated as

$$\langle V_b \rangle(t, \mathbf{r}) = \frac{\int V(t, \mathbf{r}) f(t, V, \mathbf{r}) dV}{\int f(t, V, \mathbf{r}) dV}. \quad (15)$$

During the Ostwald ripening, helium atoms released from the helium bubbles whose volume is smaller than the critical volume are absorbed by the helium bubbles whose volume is greater than the critical volume, resulting in the growth of bigger bubbles and the dissolution of smaller bubbles.

The initial condition of PBE, Eq. (4), could be calculated as

$$f(t, V, \mathbf{r})|_{t=0} = C_b(\mathbf{r}, t_{nend}) \delta \left(V - \frac{4}{3}\pi (R_b(\mathbf{r}, t_{nend}))^3 \right), \quad (16)$$

and the j th moment of the number density function f can be defined as

$$\mu_j = \int_0^\infty V^j f(V) dV. \quad (17)$$

The zeroth ($j=0$) and first ($j=1$) moments are proportional to the total density and total volume of bubbles, respectively.

3. Numerical solution of the model

3.1. Numerical solution of the rate equations of nucleation

The rate equations of the helium bubble nucleation are composed of rate equations of α -type defects, rate equations of β -type defects, and rate equations of the concentration and average radius of the helium bubbles. The solution domain and time are discretized into grids $x_i (i = 1, 2, 3, \dots, I)$, $z_k (k = 1, 2, 3, \dots, K)$, $t_l (l = 1, 2, 3, \dots, L)$, and rate equations of α -type defects are two-dimensional parabolic differential equations that could be discretized using a compact alternating direction implicit method proposed by Lele [47]. The discrete equations are written as follows:

$$\frac{(C_\alpha)_{i,k}^{l+\frac{1}{2}} - (C_\alpha)_{i,k}^l}{\Delta t} = D_\alpha \left[(g_x)_{i,k}^{l+\frac{1}{2}} + (g_z)_{i,k}^l \right] + (\dot{S}_\alpha - \dot{H}_\alpha)_{i,k}^{l+\frac{1}{2}}, \quad (18)$$

$$\frac{(C_\alpha)_{i,k}^{l+1} - (C_\alpha)_{i,k}^{l+\frac{1}{2}}}{\Delta t} = D_\alpha \left[(g_x)_{i,k}^{l+\frac{1}{2}} + (g_z)_{i,k}^{l+1} \right] + (\dot{S}_\alpha - \dot{H}_\alpha)_{i,k}^{l+\frac{1}{2}}, \quad (19)$$

where, $g_x = \frac{\partial^2 (C_\alpha)}{\partial x^2}$, $g_z = \frac{\partial^2 (C_\alpha)}{\partial z^2}$. And the g_x and g_z discretized by using the fourth-order accurate compact finite differences [48] as follows:

$$\frac{1}{10} (g_x)_{i-1,j}^n + (g_x)_{i,j}^n + \frac{1}{10} (g_x)_{i+1,j}^n = \frac{6}{5} \delta_x^2 (C_\alpha)_{i,j}^n, \quad (20)$$

and

$$\frac{1}{10} (g_z)_{i,j-1}^n + (g_z)_{i,j}^n + \frac{1}{10} (g_z)_{i,j+1}^n = \frac{6}{5} \delta_z^2 (C_\alpha)_{i,j}^n, \quad (21)$$

where, $\delta_x^2 (C_\alpha)_{i,j}^n = \frac{1}{\Delta x^2} ((C_\alpha)_{i-1,j}^n - 2(C_\alpha)_{i,j}^n + (C_\alpha)_{i+1,j}^n)$, $\delta_z^2 (C_\alpha)_{i,j}^n = \frac{1}{\Delta z^2} ((C_\alpha)_{i,j-1}^n - 2(C_\alpha)_{i,j}^n + (C_\alpha)_{i,j+1}^n)$. Eqs. (18) and (19) are tridiagonal equations that could be solved using the Thomas method.

The unified differential format of the rate equations of the β -type defects is written as

$$\frac{(C_\beta)_{i,k}^{l+\frac{1}{2}} - (C_\beta)_{i,k}^{l-\frac{1}{2}}}{\Delta t} = (\dot{S}_\beta - \dot{H}_\beta)_{i,k}^l. \quad (22)$$

The discretization method for the Eqs. (2-A), (2-b) and (2-c) is consistent with Eq. (22), and after solving Eqs. (18) and (19) and determining the concentration of the α -type defects at each time step, the other discrete equations can be solved by the step iteration.

3.2. Numerical solution of the population balance equation

The population balance Eq. (4) is a differential-integral equation, the bubble coalescence term on the right side of Eq. (4) is discretized using the cell average technique [49], and the bubble volume domain is discretized into several cells $[V_{n-\frac{1}{2}}, V_{n+\frac{1}{2}}]$ ($n = 1, 2, 3, \dots, M$) with a representative volume $V_n = \frac{(V_{n-\frac{1}{2}} + V_{n+\frac{1}{2}})}{2}$ at each cell. In each cell, the density distribution function of the bubble volume can be approximated in terms of Dirac-delta distributions as

$$f(V) \approx N_n \delta(V - V_n), \quad (23)$$

thus

$$N_n = \int_{V_{n-\frac{1}{2}}}^{V_{n+\frac{1}{2}}} f(V) dV. \quad (24)$$

After integrating the population balance Eq. (4) over each sub-cell and applying Eq. (24) to the integrated equation, Eq. (25) is obtained as follow:

$$\frac{\partial N_n(x, z)}{\partial t} + (\bar{v}_b)_n \left(\frac{\partial N_n(x, z)}{\partial x} + \frac{\partial N_n(x, z)}{\partial z} \right) = B_n - D_n, \quad (25)$$

where, the expression of the coalescence source term B_n is

$$B_n = \left| \frac{1}{2} \int_{V_{n-\frac{1}{2}}}^{V_{n+\frac{1}{2}}} dV \int_{V_0}^V c(\xi, V - \xi) f(x, z, \xi) f(x, z, V - \xi) d\xi \right| \\ = \left| \sum_{\substack{m \geq m' \\ m, m'}} \left(1 - \frac{1}{2} \delta_{m, m'}\right) c(V_m, V_{m'}) N_m(x, z) N_{m'}(x, z) \right|_{V_{n-1} \leq V_m + V_{m'} \leq V_{n+1}} \quad (26)$$

and the expression of coalescence sink term D_n is

$$D_n = \left| \int_{V_{n-\frac{1}{2}}}^{V_{n+\frac{1}{2}}} N_n(x, z) \delta(V - V_n) dV \right. \\ \left. + \sum_{m=1}^M \int_{\xi_{m-\frac{1}{2}}}^{\xi_{m+\frac{1}{2}}} c(V, \xi) N_m(x, z) \delta(V - V_m) d\xi \right| \\ = \left| N_n(x, z) \sum_{m=1}^M c(V_n, V_m) N_m(x, z) \right| \quad (27)$$

The coalescence source term needs to be redistributed when the volume of the newborn bubble formed by coalescence does not match the representative volume. The volume of the newborn bubble is defined to be \bar{V}_n , and it is assumed that $\bar{V}_n > V_n$, thus the following equations need to be satisfied for the distribution weight coefficients a_1 and a_2 due to volume conservation:

$$a_1(\bar{V}_n, V_n)V_n + a_2(\bar{V}_n, V_n)V_{n+1} = B_n\bar{V}_n \\ a_1(\bar{V}_n, V_n) + a_2(\bar{V}_n, V_n) = B_n \quad (28)$$

The distribution weight coefficients a_1, a_2 are, respectively, determined by Eq. (28) to be $a_1 = B_n\lambda_n^+(\bar{V}_n)$ and $a_2 = B_n\lambda_{n+1}^-(\bar{V}_n)$, where $\lambda_n^\pm(V) = \frac{V - V_{n\pm1}}{\bar{V}_n - V_{n\pm1}}$.

The redistributed coalescence source term B_n^{RE} of the n th cell could be written as

$$B_n^{\text{RE}} = |B_{n-1}\lambda_n^-(V)H(\bar{V}_{n-1} - V_{n-1}) + B_n\lambda_n^-(\bar{V}_n)H(V_n - \bar{V}_n) \\ + B_n\lambda_n^+(\bar{V}_n)H(\bar{V}_n - V_n) + B_{n+1}\lambda_{n+1}^+(\bar{V}_{n+1})H(V_{n+1} - \bar{V}_{n+1})| \quad (29)$$

where, the function $H(x)$ is defined as $H(x) = \begin{cases} 1, & |x| > 0 \\ 0.5, & |x| = 0 \\ 0, & |x| < 0 \end{cases}$

The initial condition of the population balance equation also needs to be redistributed when the cell average technique is used, and Eq. (16) could be rewritten as

$$N_{n_0} = C_{b0}\lambda_{n_0}^-(V_{b0})H(V_{n_0} - V_{b0}) + C_{b0}\lambda_{n_0}^+(V_{b0})H(V_{b0} - V_{n_0}) \\ N_{n_0-1} = C_{b0}\lambda_{n_0-1}^+(V_{b0})H(V_{n_0} - V_{b0}) \\ N_{n_0+1} = C_{b0}\lambda_{n_0+1}^-(V_{b0})H(V_{b0} - V_{n_0}) \quad (30)$$

where, $V_{b0} = \frac{4}{3}\pi(R_b(\mathbf{r}, t_{nend}))^3$, n_0 is the numbering of volume cell where V_{b0} is located, and $C_{b0} = C_b(\mathbf{r}, t = t_{nend})$ is the concentration of helium bubbles at the end of nucleation.

The bubble migration term is discretized by the finite difference method, and the direction of the helium bubble motion is then determined by random sampling in discrete directions. The

time derivative in Eq. (4) is discretized as $\frac{\partial N_n}{\partial t} = \frac{(N_n)^{t+1/2} - (N_n)^{t-1/2}}{\Delta t}$, and a diamond differential auxiliary relation: $2(N_n)^t = (N_n)^{t+1/2} + (N_n)^{t-1/2}$ is applied to make Eq. (4) closed.

Then the discrete form of the population balance Eq. (4) with migration and coalescence terms is written as Eq. (31):

$$\frac{(N_n)^{t+1/2} - (N_n)^{t-1/2}}{\Delta t} \\ + (\bar{v}_b)_n \left(\kappa \frac{(N_n)_{i+\frac{1}{2}, k} - (N_n)_{i-\frac{1}{2}, k}}{\Delta x} + \zeta \frac{(N_n)_{i, k+\frac{1}{2}} - (N_n)_{i, k-\frac{1}{2}}}{\Delta z} \right) \\ = B_{n-1}\lambda_n^-(\bar{V}_{n-1})H(\bar{V}_{n-1} - V_{n-1}) \\ + B_n\lambda_n^-(\bar{V}_n)H(V_n - \bar{V}_n) + B_n\lambda_n^+(\bar{V}_n)H(\bar{V}_n - V_n) \\ + B_{n+1}\lambda_{n+1}^+(\bar{V}_{n+1})H(V_{n+1} - \bar{V}_{n+1}) - (N_n)_{i, k} \sum_{m=1}^M c(V_n, V_m)(N_m)_{i, k}. \quad (31)$$

The process described by the bubble growth term \dot{V} is essentially the absorption or release of point defects by an individual bubble. However, there is a lack of information on the size of defects and helium atoms in the growth term, thus it is difficult to establish the absorption or release kernel functions for point defects and bubbles in the same way as the kernel functions for bubble coalescence. Therefore, the cell average technique is not suitable for the discretization of the bubble growth term in this paper. To overcome this difficulty, the bubble growth term is solved using a Lagrange plus remap approach while obtaining accurate numerical results.

The basic steps of the Lagrange plus remap approach are:

- (1) Population balance equation with migration and coalescence terms are solved using the cell average technique under a fixed discrete volume grid Γ^a , and the corresponding distribution $N_n^{\text{old}}(\Gamma^a)$ is obtained.
- (2) A shifted volume grid Γ^b is obtained by applying Eq. (32) to the endpoints and representative points of the cells on Γ^a , and the corresponding distribution of the volume grid Γ^b is $N_n^{\text{old}}(\Gamma^b)$.

$$\frac{dV_n}{dt} = \dot{V}(V_n) \\ \frac{dV_{n-\frac{1}{2}}}{dt} = \dot{V}(V_{n-\frac{1}{2}}). \quad (32)$$

- (3) The distribution $N_n^{\text{old}}(\Gamma^b)$ is remapped to the initial grid Γ^a according to the total volume conservation and polygon intersection algorithm, resulting in a new distribution $N_n^{\text{new}}(\Gamma^a)$.

Since it eventually returns to the initial volume grid discretized by the cell average technique, the Lagrange plus remap approach can be combined with the cell average technique to solve the complete population balance (Eq. (4)).

4. Results and discussion

The bubble density n_b , average bubble diameter $\langle d_b \rangle$ and size distribution of helium bubbles are the focus of the following verification and discussion. In the present work, n_b is equal to μ_0 whose expression is given by Eq. (11), and $\langle d_b \rangle$ is the statistical average of the bubble diameter distribution. And for the convenience of comparison, the size distributions of helium bubbles obtained from simulations and experimental statistics are normalized to the probability density distributions of helium bubble diameter.

Table 1
Material parameters for Mo used in numerical calculations.

Notation	Description	value	Refs.
a_0	Lattice Constant	3.16 Å	[50]
Ω	Atomic Volume	1.562×10^{-29} m ³	–
E_m^i	SIA Migration Energy	0.064 eV	[51]
E_v^i	Vacancy Migration Energy	1.25 eV	[52]
E_{He}^i	Helium Migration Energy	0.06 eV	[50]
E_f^i	SIA Formation Energy	8.77 eV	[53]
E_f^v	Vacancy Formation Energy	2.96 eV	[53]
E_b^{2g}	Di-Helium Interstitial Binding Energy	1.03 eV *	[54]
$E_b^{v,g}$	Helium Substitutional Binding Energy	4.57 eV *	[54]
$E_b^{v,2g}$	Di-Helium Substitutional Binding Energy	6.65 eV *	[54]
v_i	SIA Attempt Frequency	6×10^{12} Hz *	[55]
v_v	Vacancy Attempt Frequency	6×10^{12} Hz *	[55]
v_{He}	Helium Attempt Frequency	6×10^{10} Hz *	[55]
b	Re-solution Parameter	1	[36]
s_f	Recombination Survival Fraction	0.25	[20]
ρ	Dislocation Density	3×10^{14} m/m ⁻³	[56]
ω_i	SIA Bias Factor	1.4	[20]
ω_v	Vacancy Bias Factor	1	[20]
D_0	Pre-exponential factor of the surface diffusion coefficient	8×10^{-3} cm ² /s	–
E_S	Surface activation energy	2.17 eV	–

* the material parameter for W.

4.1. Model validation: reproduce experimental data of helium bubbles

To validate the theoretical model in this paper, the simulation results of the theoretical model are compared with the experimental observations reported in Refs. [29,30]. The helium bubble size distribution in irradiated Mo at 673 K reported in Ref. [29] is used as reference data to validate the nucleation part of the model in this paper. And the bubble size distribution in Mo was obtained by *in-situ* transmission electron microscopy irradiated by 30 keV He⁺ with a flux of 6.6×10^{12} ions/(cm²·s). The bubble density n_b , average bubble diameter $\langle d_b \rangle$ and size distributions of helium bubbles in FeCrAl obtained by *in-situ* TEM observation during the stepwise annealing process reported in Ref. [30] are used as the validation data for the present coupling model. The FeCrAl alloy was pre-irradiated by 30 keV He⁺ with a flux of 2.38×10^{13} ions/(cm²·s) for 30 min before annealing.

The results of helium and point defect deposition in Mo and FeCrAl alloy are calculated by using the SRIM program in the full Damage Cascades mode with a 0° incidence angle. The displacement energy (E_d) of Mo, Fe, Cr and Al are set as 25, 40, 40, and 25 eV, respectively.

The following simulation conditions and domains are adopted for model validation and discussion. The spatial grid step is set to $\Delta x = \Delta z = 5$ nm, and the total spatial grid size is matched to the rounded maximum depth of helium ion deposition calculated by SRIM. The time step Δt in the simulation of PBE is set to 1 s in the present work, while Δt in the simulation of RE needs to be adjusted according to the temperature and material parameters to ensure the stability of the numerical solution of Eqs. (18) and (19). And it should be mentioned that in simulations of PBE, the volume domain is discretized geometrically into 50 cells by the rule $V_{n+1/2} = 1.2V_{n-1/2}$, and $V_{1/2} = \frac{4\pi}{30}$ nm³.

The important material parameters involved in the model validation and discussion section of this paper are listed in Tables 1 and 2. We adopt partial data calculated in W to supplement the inadequate coverage of material parameters of Mo in the literature, as listed in Table 1.

Since there is no established set of parameters for FeCrAl alloy in the literature that covers the energetics of relevant defects, we adopt the data measured or calculated in bcc iron for defect formation and migration energies and blinding energies of reactions between defects, as listed in Table 2.

Fig. 2 shows the comparison of the probability density distributions of the bubble diameter during irradiation obtained by RE simulation and TEM, where Fig. 2 (a) corresponds to an irradiation time of 70 min and Fig. 2 (b) corresponds to an irradiation time of 140 min. It can be seen from Fig. 2 (b) that the simulated helium bubble size is slightly larger than the experimental statistical one, and the simulation results are in good agreement with the experimental statistics in general. However, the simulated helium bubble distribution in Fig. 2 (a) is more concentrated than the experimental statistical distribution. The possible reason for this deviation is that the initial condition of Eq. (2-C) is a fixed value, so the size distribution obtained by the simulation is not dispersed enough when the irradiation time is insufficient.

The simulation process and parameters involved in the validation of the combined model in this paper are shown in Fig. 3. The simulation process can be divided into four stages in sequence: I. simulation of the nucleation results of the helium bubbles with irradiation at 300 K using the rate equations (irradiation energy is 30 kV with a flux of 2.38×10^{13} ions/(cm²·s)), II. simulation of further nucleation and growth of helium bubbles at 673 K and 773 K in sequence without generation of helium and vacancy, III. simulation of helium bubble coarsening at 873 K and 973 K in sequence by PBE, IV. simulation of the further coarsening of helium bubbles at 1073 K by PBE. The heating time during annealing is neglected in the simulations compared to the experimental procedure in Ref. [30].

The diffusion of thermal vacancies is the driving factor for the continuous growth of helium bubbles due to the absorption of thermal vacancies and is also the driving factor for the OR mechanism. And the OR mechanism will only work at sufficiently high annealing temperatures [27] and the higher internal pressure of the smaller bubbles would suppress the OR mechanism [58]. Therefore, it is assumed in this paper that the main mechanisms controlling the bubble coarsening at stage III in Fig. 3 are MC and the continuous growth, while the coarsening of helium bubbles at stage IV in Fig. 3 is driven by OR and MC.

Fig. 4 shows the comparison of $\langle d_b \rangle$, n_b and the probability density distributions of the bubble diameter obtained by PBE simulation and TEM. As shown in Fig. 4 (a), $\langle d_b \rangle$ predicted by PBE simulation are in good agreement with the experimental statistics, and the relative errors of $\langle d_b \rangle$ at the three temperatures are all less than 10%. It can be seen from Fig. 4 (b) that n_b predicted

Table 2
Material parameters for bcc iron used in numerical calculations.

Notation	Description	value	Refs.
a_0	Lattice Constant	2.866 Å	–
Ω	Atomic Volume	$1.562 \times 10^{-29} m^3$	–
E_m^i	SIA Migration Energy	0.34 eV	[1, 57]
E_m^v	Vacancy Migration Energy	0.67 eV	[1, 57]
E_m^{He}	Helium Migration Energy	0.06 eV	[57]
E_f^i	SIA Formation Energy	3.77 eV	[1]
E_f^v	Vacancy Formation Energy	2.07 eV	[1]
$E_{f,g}^{2g}$	Di-Helium Interstitial Binding Energy	0.43 eV	[57]
$E_b^{v,g}$	Helium Substitutional Binding Energy	2.30 eV	[57]
$E_b^{v,2g}$	Di-Helium Substitutional Binding Energy	3.71 eV	[57]
v_i	SIA Attempt Frequency	$6 \times 10^{12} \text{ Hz}$	[55]
v_v	Vacancy Attempt Frequency	$6 \times 10^{12} \text{ Hz}$	[55]
v_{He}	Helium Attempt Frequency	$6 \times 10^{10} \text{ Hz}$	[55]
b	Re-solution Parameter	1	[36]
s_f	Recombination Survival Fraction	0.25	[20]
ρ	Dislocation Density	$2 \times 10^{12} \text{ m/m}^{-3}$	[56]
ω_i	SIA Bias Factor	1.4	[20]
ω_v	Vacancy Bias Factor	0.25	–
D_0	Pre-exponential factor of the surface diffusion coefficient	$5.8 \times 10^{-3} \text{ cm}^2/\text{s}$	–
E_S	Surface activation energy	1.3575 eV	–

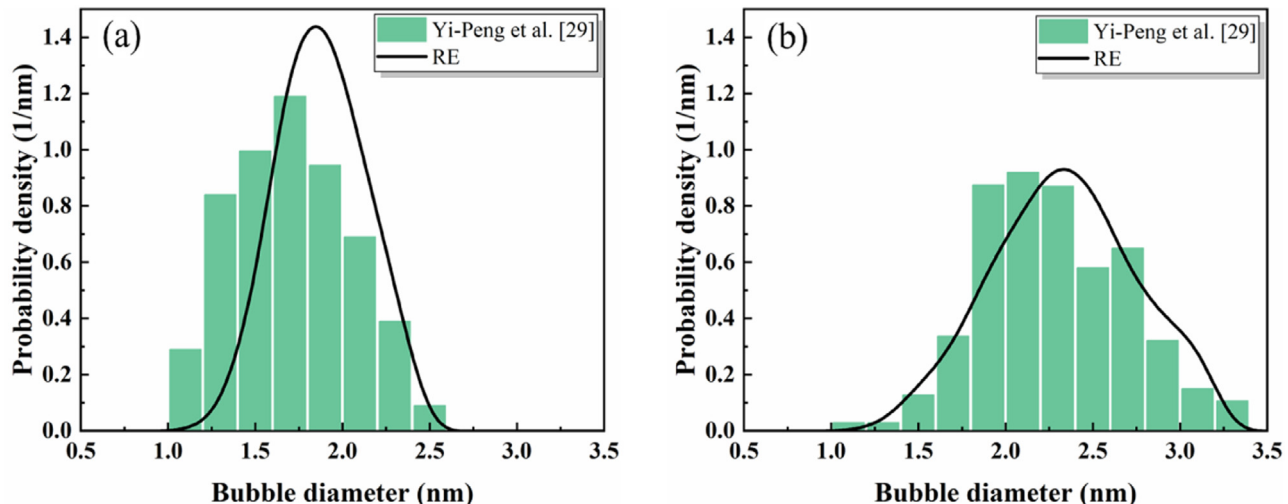


Fig. 2. Comparison of the experimental TEM statistics and simulation results of the probability density distribution of helium bubble diameter in Mo irradiated by 30 keV He^+ with a flux of $6.6 \times 10^{12} \text{ ions}/(\text{cm}^2 \cdot \text{s})$ at 673 K after different fluence irradiation: (a) $2.77 \times 10^{16} \text{ ions}/\text{cm}^2$, (b) $5.74 \times 10^{16} \text{ ions}/\text{cm}^2$. Experimental data were reported by Chen et al. [29].

by the model is generally larger than the experimental value. And n_b predicted by the model at 1073 K is in good agreement with the experimental statistics while the prediction errors of n_b are greater at the lower annealing temperatures of 873 K and 973 K. There are two possible reasons for this deviation. Experimentally, the proportion of small-sized bubbles is larger at lower temperatures, and counting the number of small-sized bubbles is challenging, resulting in small statistical results of TEM observation. On the other hand, the reduction in the number density of helium bubbles caused by the heating process is neglected in the simulation process, which leads to a generally high density of helium bubbles predicted by PBE simulation. It can be seen from Fig. 4 (c) and (d) that the trend and range of the probability density distribution of bubble diameter predicted by the model are consistent with the trend and range of the experimentally statistical distribution. The model generally captures the main features of helium bubble evolution and is particularly effective for reproducing the coarsening of helium bubbles at high annealing temperatures. It can also be deduced that the assumptions made in this paper for the govern-

ing mechanisms of helium bubble evolution at various temperatures are reasonable.

4.2. Effect of irradiation parameters on the evolution of helium bubbles

The irradiation energy and flux are not parameters in the present model, but changing the irradiation parameters will change the generation rate of helium (G_{He}) and vacancy (G_{Vac}) involved in the nucleation part of the model, thereby affecting the evolution of helium bubbles. The range of the irradiation energy discussed in this paper is 10 kV ~ 100 kV, which avoids the variance of the nucleation and evolution mechanism of helium bubbles due to low irradiation energy [21].

Fig. 5 (a) and (b) show the average generation rate of helium ($\langle G_{He} \rangle$), the average generation rate of vacancy ($\langle G_{Vac} \rangle$) and the average value of the ratio of the two generation rates ($\langle G_{He}/G_{Vac} \rangle$) as a function of the irradiation energy. As shown in Fig. 5 (a), $\langle G_{He} \rangle$ and

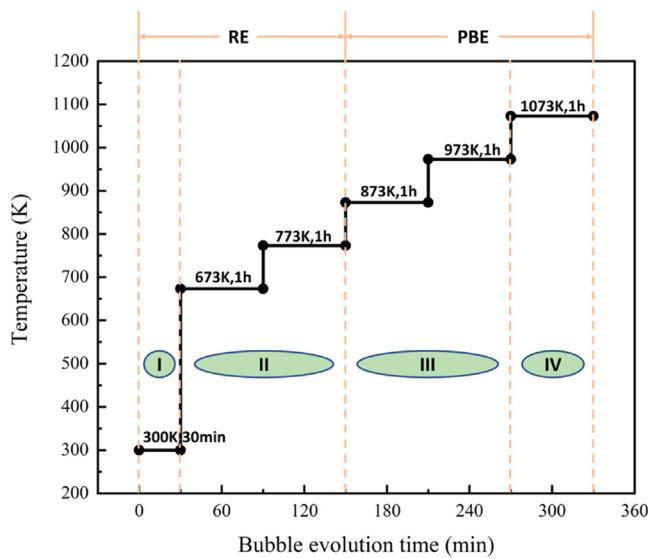


Fig. 3. The simulation process and parameters involved in the experimental validation of the present combined model. The inset describes the four main simulation stages separated by the dashed vertical lines.

$\langle G_{\text{He}} \rangle$ both decrease and tend to be stable with the increase of irradiation energy. And it can be seen from Fig. 5 (b) that the change of $\langle G_{\text{He}}/G_{\text{Vac.}} \rangle$ with the energy can be divided into three different phases. The ratio decreases sharply with the increase of energy in the range of 10 kV ~ 30 kV, then rises to a certain extent in the range of 30 kV ~ 40 kV, and finally decreases to a stable value in the range of 40 kV ~ 100 kV. Fig. 5 (c) shows the simulation results of $\langle d_b \rangle$ and n_b after the bubble nucleation with rising irradiation energy at stage I and stage II in Fig. 3, and the irradiation fluence is fixed at 4×10^{16} ion/cm² with a irradiation time of 30 min. It can be seen that the variation trend of n_b with irradiation energy is consistent with that of $\langle G_{\text{He}}/G_{\text{Vac.}} \rangle$ reflected in Fig. 5 (b). It can be reasonably inferred from the rate equations that the larger the value of $G_{\text{He}}/G_{\text{Vac.}}$, is, the more dominant the nucleation effect of helium bubbles during the irradiation process is, leading to a larger density and a smaller size of the nucleated helium bubbles. Conversely, the smaller the value of $G_{\text{He}}/G_{\text{Vac.}}$, is, the more dominant the continuous growth of helium bubbles described by Eq. (2-C) is, resulting in a lesser density and a bigger size of the nucleated helium bubbles.

The evolution of $\langle d_b \rangle$ and n_b during a stepwise annealing process corresponding to stage III and stage IV in Fig. 3 after nucleation with different irradiation energies are shown in Fig. 6 (a) and

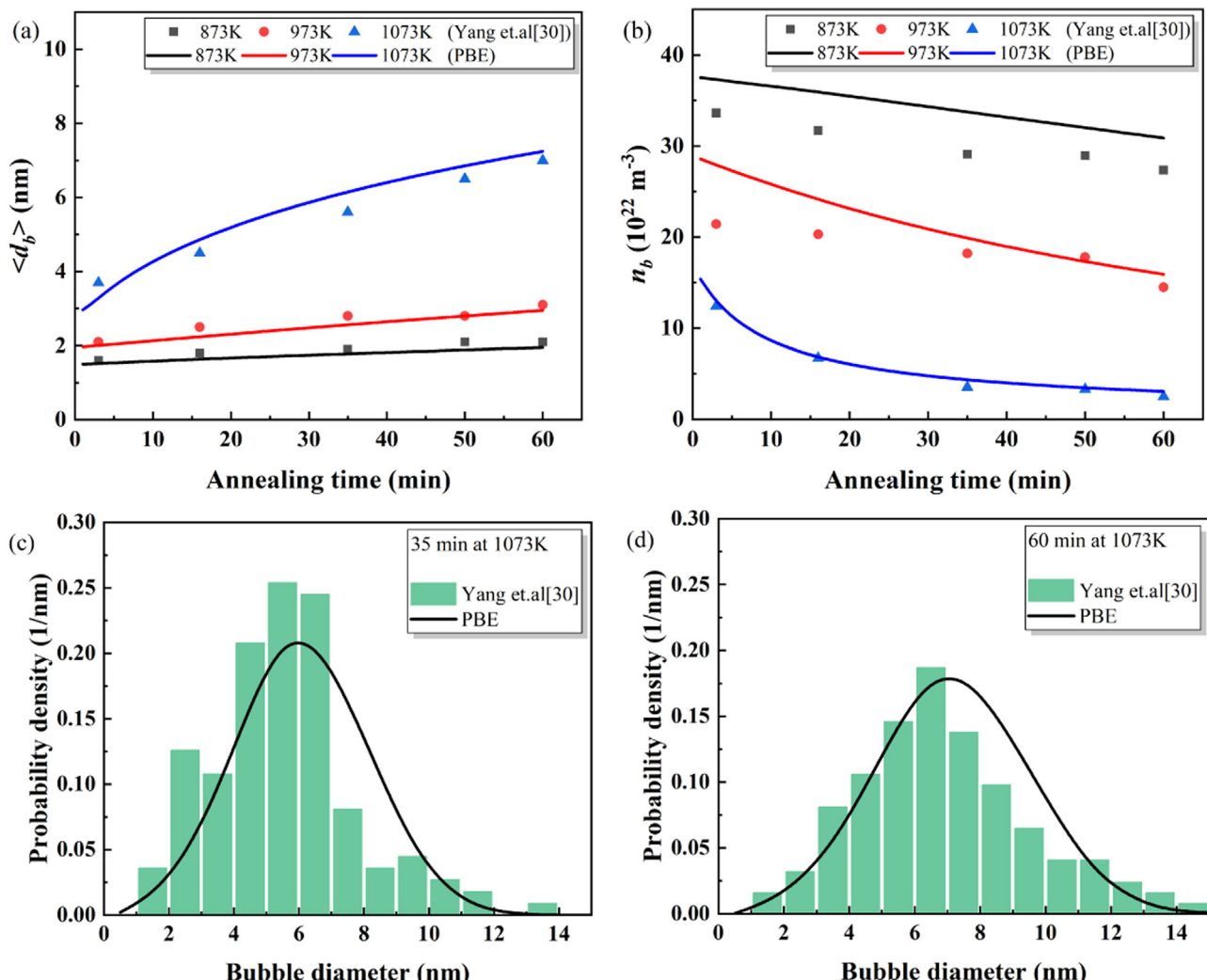


Fig. 4. Comparison of the experimental and simulation results of the density and size information during helium bubble evolution in FeCrAl: (a) $\langle d_b \rangle$ vs. annealing time at different annealing temperatures; (b) n_b vs. annealing time at different annealing temperatures; (c) and (d) the probability density distribution of helium bubble diameter in the pre-irradiated FeCrAl alloys annealed at 1073 K for 35 min and 60 min. Experimental data were reported by Tavassoli [30].

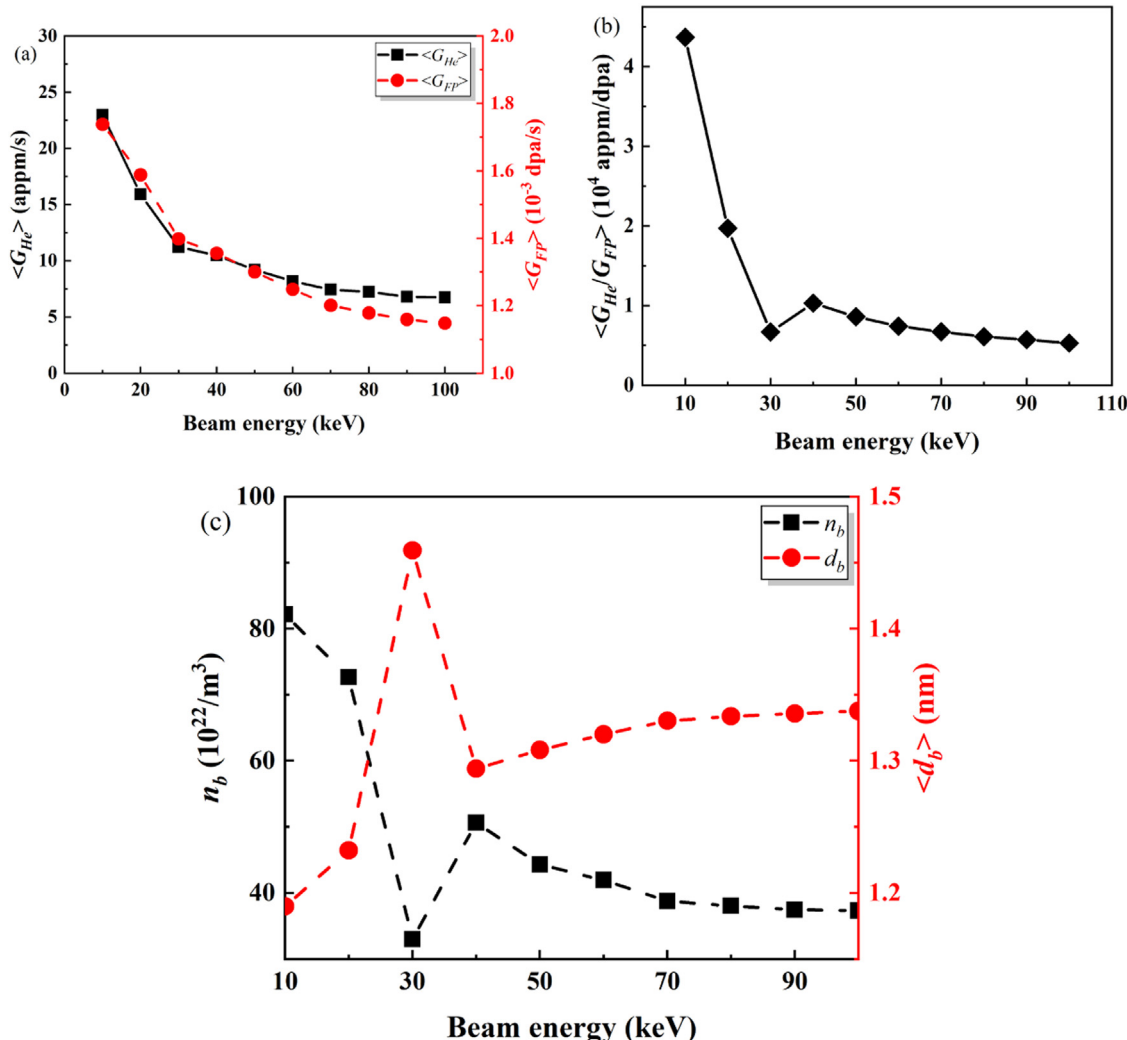


Fig. 5. The results of SRIM simulations of ion deposition and RE simulations of bubble nucleation with irradiation energy: (a) the average generation rate of helium ($\langle G_{He} \rangle$) and vacancy ($\langle G_{Vac.} \rangle = s_f \langle G_{FP} \rangle$); (b) the average value of the ratio of the two generation rates ($\langle G_{He}/G_{Vac.} \rangle$); (c) density and average diameter of helium bubbles after nucleation.

(b), respectively. In the early period of annealing, the growth rate of $\langle d_b \rangle$ and the decay rate of n_b corresponding to the irradiation energy of 10 kV are much larger than that corresponding to other higher irradiation energies, resulting in intersections between the evolution process of 10 kV and the evolution processes of other higher irradiation energies. The reason for the intersection is that the high nucleation density and low nucleation size will lead to an enhanced coalescence effect between the helium bubbles, resulting in an intensified transition from helium bubble density decay to helium bubble size growth. The relative magnitudes of the helium bubble density corresponding to the three energies do not change again after 70 min. At the end of the evolution, $\langle d_b \rangle$ decreases with rising irradiation energy, while n_b increases with the rise of the irradiation energy. The variation trends of the value of $\langle d_b \rangle$ and n_b at the end of the evolution with irradiation energy are given in Fig. 6 (c). As shown in Fig. 6 (c), $\langle d_b \rangle$ gradually decreases and tends to be stable with the increase of irradiation energy, which is consistent with the variation trend of $\langle G_{He} \rangle$ and $\langle G_{Vac.} \rangle$ reflected in Fig. 5 (a). Combining the evolution of $\langle d_b \rangle$ and n_b corresponding to different irradiation energies shown in Fig. 6 (a) and (b). It can be reasonably concluded that the final size of the helium bubble population is positively correlated with the most initial input of irradiation defects after the coalescence between helium bubbles during annealing.

The irradiation flux does not affect the calculation results of SRIM, but it can be seen from Eqs. (3-A) and (3-b) that $\langle G_{He} \rangle$ and $\langle G_{Vac.} \rangle$ are proportional to the irradiation flux, and $\langle G_{He}/G_{Vac.} \rangle$ is independent of the irradiation flux.

The irradiation time is fixed at 30 min when discussing the effect of irradiation flux on the evolution of helium bubbles. Fig. 7 (a) and (b) show the evolution of $\langle d_b \rangle$ and n_b during a stepwise annealing process corresponding to stage III and stage IV in Fig. 3 after the nucleation at the same irradiation energy of 30 kV with different irradiation fluences. It can be seen that the evolution processes of $\langle d_b \rangle$ and n_b corresponding to different irradiation fluences no longer intersect, and the relative magnitudes of the irradiation fluences determine the relative magnitudes of the helium bubble size and density in the evolution process. This is because the density and size of the nucleated helium bubble after irradiation increase with rising irradiation flux, making the bubble coalescence effect during annealing comparable for each irradiation flux. The variation trend of the evolution results of $\langle d_b \rangle$, n_b , and μ_1 with irradiation flux are given in Fig. 7 (c). As shown in Fig. 7 (c), $\langle d_b \rangle$ and n_b grow nonlinearly with the increase of the irradiation flux, and the growth rate decreases continuously. And μ_1 increases approximately linearly with rising irradiation fluences. Since μ_1 is proportional to the total volume of helium bubbles, it can be concluded that the total volume of the evolved helium bub-

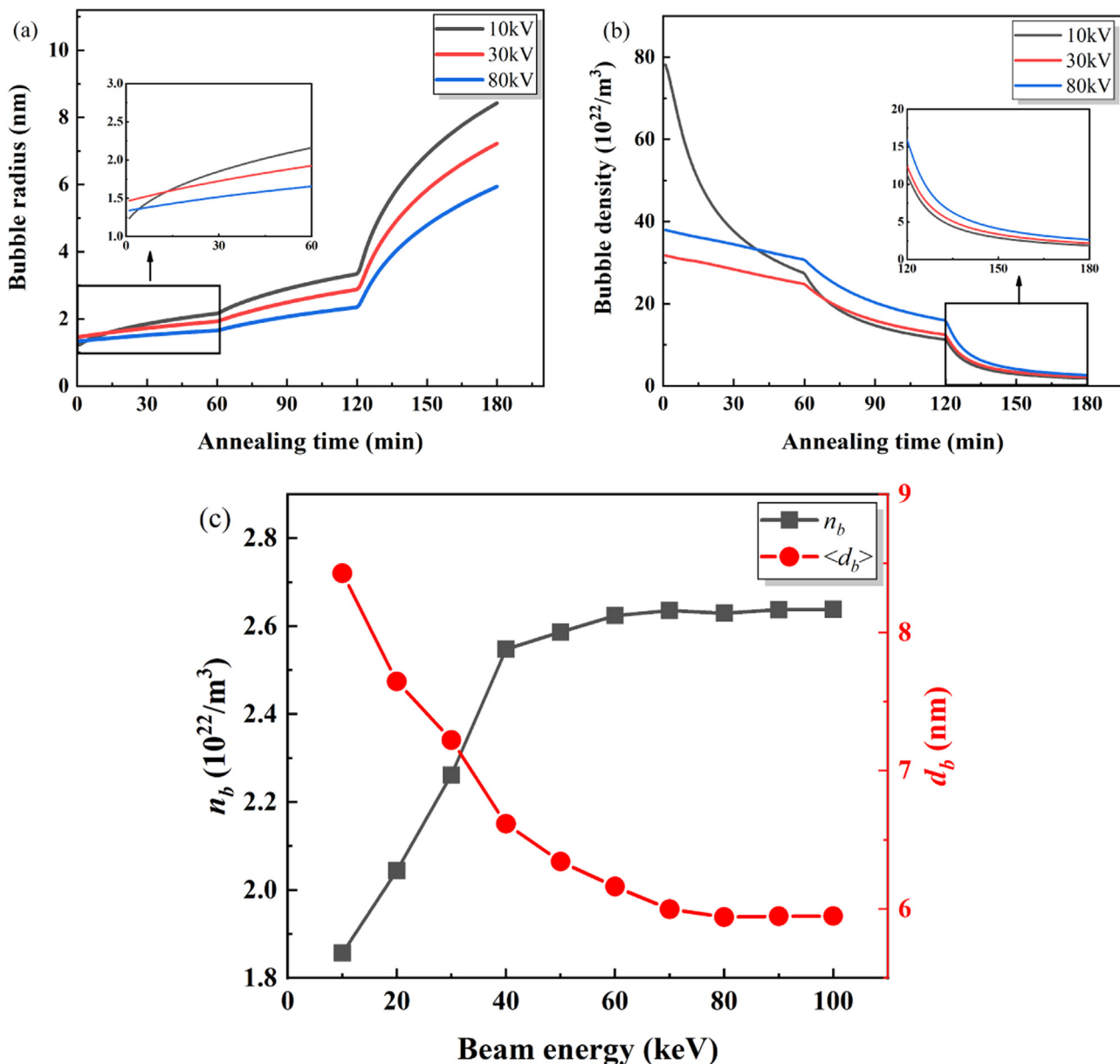


Fig. 6. The evolution of (a) $\langle d_b \rangle$ and (b) n_b during a stepwise annealing process corresponding to stage III and stage IV in Fig. 3 simulated by PBE for different irradiation energy; (c) The simulated results of $\langle d_b \rangle$ and n_b vs. irradiation energy after bubble coarsening under a stepwise annealing process corresponding to stage III and stage IV in Fig. 3.

bles is proportional to the irradiation flux when irradiation time is fixed.

4.3. Effect of coarsening mechanisms on the evolution of helium bubbles

In this section and Section 4.4, the irradiation parameters are kept consistent with the experimental [30]. The comparisons of $\langle d_b(t) \rangle$, $n_b(t)$ and the final probability density distribution of bubble diameter when bubble coarsening is driven by MC, OR, and MC plus OR (MC+OR) at 1073 K are shown in Fig. 8. It can be seen from Fig. 8 (a) that the growth of $\langle d_b \rangle$ for MC+OR is significantly larger than that for MC and OR, respectively, so the combined effect of MC and OR is positive for the growth of $\langle d_b \rangle$. As shown in Fig. 8 (b), the decay rate of n_b for MC is always slower than that for OR and MC+OR, and the decay rate of n_b for MC+OR is higher

than that for OR at the initial period of coarsening. However, n_b for MC+OR decrease slowly in the middle and late periods of annealing, gradually coinciding with n_b for OR.

As shown in Fig. 8 (c), the probability densities of helium bubbles in the initial bubble region in the case of the three mechanisms decrease significantly, while the number of helium bubbles with larger sizes outside the initial region increases significantly, which is the reason for the rise in $\langle d_b \rangle$ in Fig. 8 (a). And the evolutionary completed probability densities of bubble diameter in the case of OR and MC+OR are approximately normally distributed, while the distribution for MC exhibits a positively skewed distribution.

The causes of the final helium bubble size distribution differed for the three coarsening mechanisms. When the coarsening of helium bubbles is only governed by MC, the helium bubbles in the initial bubble region coalesce to form larger-sized helium bub-

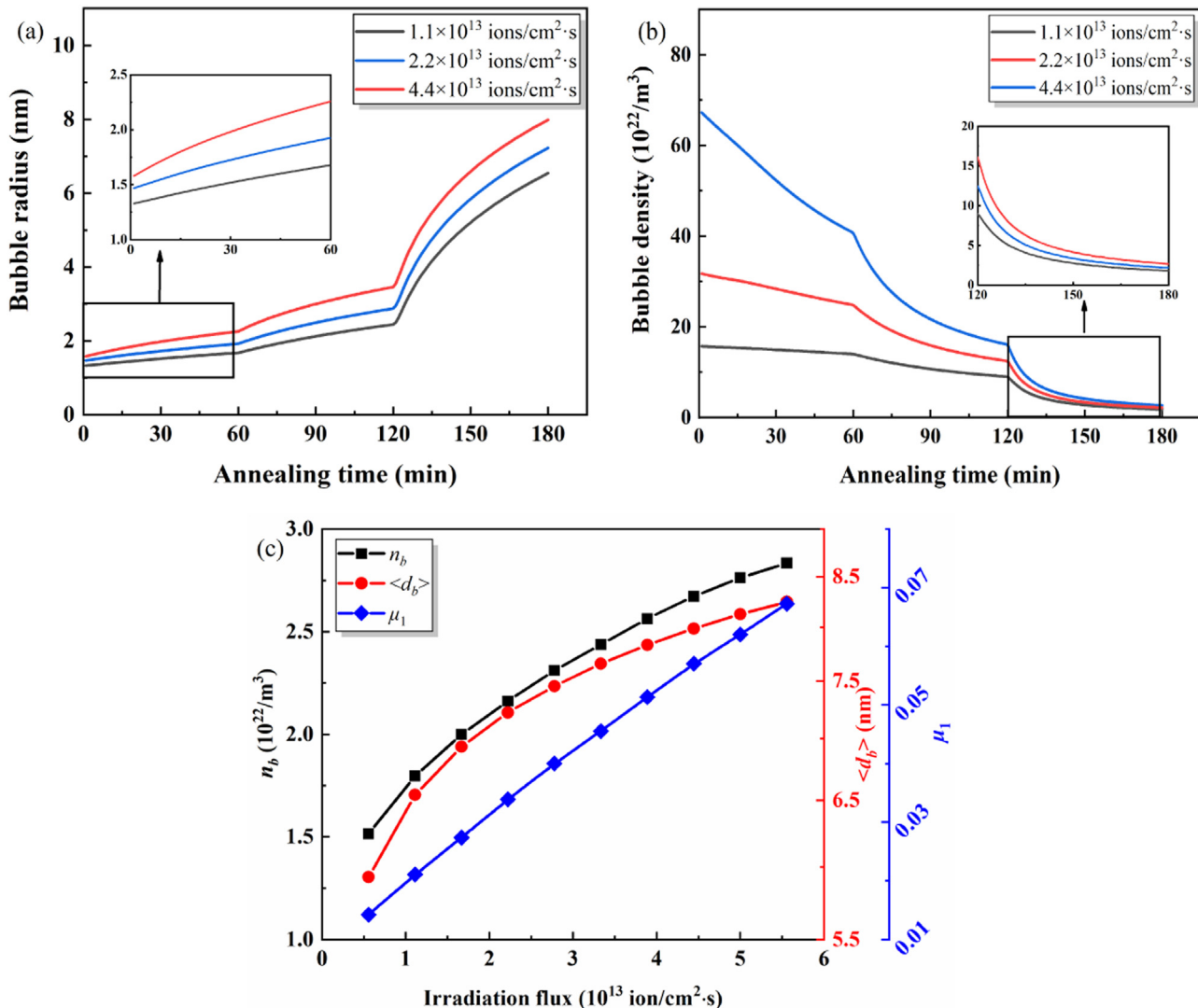


Fig. 7. The evolution of (a) $\langle d_b \rangle$ and (b) n_b during a stepwise annealing process corresponding to stage III and stage IV in Fig. 3 simulated by PBE for different irradiation flux; (c) The simulation results of $\langle d_b \rangle$, n_b and μ_1 vs. irradiation flux after the bubble evolution under a stepwise annealing process corresponding to stage III and stage IV in Fig. 3.

bles outside the distribution, resulting in the transfer of probability density from the initial bubble region to the larger bubble region. However, the skewed size distribution for MC suggests that the one-hour coalescence of helium bubbles at 1073 K is not sufficient. And when the helium bubble coarsening is only driven by OR, helium bubbles whose sizes are larger than the average size of bubbles expand, while the helium bubbles smaller than the average bubble shrink. Therefore, the size distribution of helium bubbles will continuously extend to both sides, with the average size of the current helium bubble population as the dividing line. And the shrinking helium bubbles disappear when they are smaller than the smallest helium bubble counted in the simulation, resulting in a continuous reduction in the density of small-sized helium bubbles. In addition to the respective roles of MC and OR on helium bubble evolution described above, there are links between MC and OR when both MC and OR participate in the control of the coarsening of helium bubbles. On the one hand, the shrinkage of small-sized helium bubbles and the expansion of large-sized helium bubbles caused by OR provide conditions for more intense helium bubble coalescence, leading to a further increase in the number of large-sized helium bubbles and a decrease in the number of small-

sized helium bubbles. On the other hand, MC inhibits the disappearance of the shrinking helium bubbles caused by the OR mechanism to a certain extent, making n_b for MC+OR not significantly reduced compared to that for OR. It can be seen from Fig. 8 (b) that the decay rate of n_b in the case of MC+OR is progressively slower, which indicates that the combined effect of MC and OR is gradually emerging in the helium bubble coarsening.

4.4. Effect of annealing parameters on the evolution of helium bubbles

Fig. 9 (a) and (b) show the evolutions of $\langle d_b \rangle$ and n_b simulated by PBE during annealing at different temperatures in stage IV of Fig. 3. As shown in Fig. 9 (a) and (b), $\langle d_b(t) \rangle$ is monotonically increasing functions of time t , while $n_b(t)$ is monotonically decreasing function of t for each temperature. And the growth of $\langle d_b \rangle$ and the decay of n_b will both increase significantly as the temperature rises. This is because the diffusion coefficient of the helium atom and thermal vacancy and the motion velocity of helium bubbles will increase at elevated temperatures, and the concentration of thermal vacancy will be greater at a higher temperature, resulting

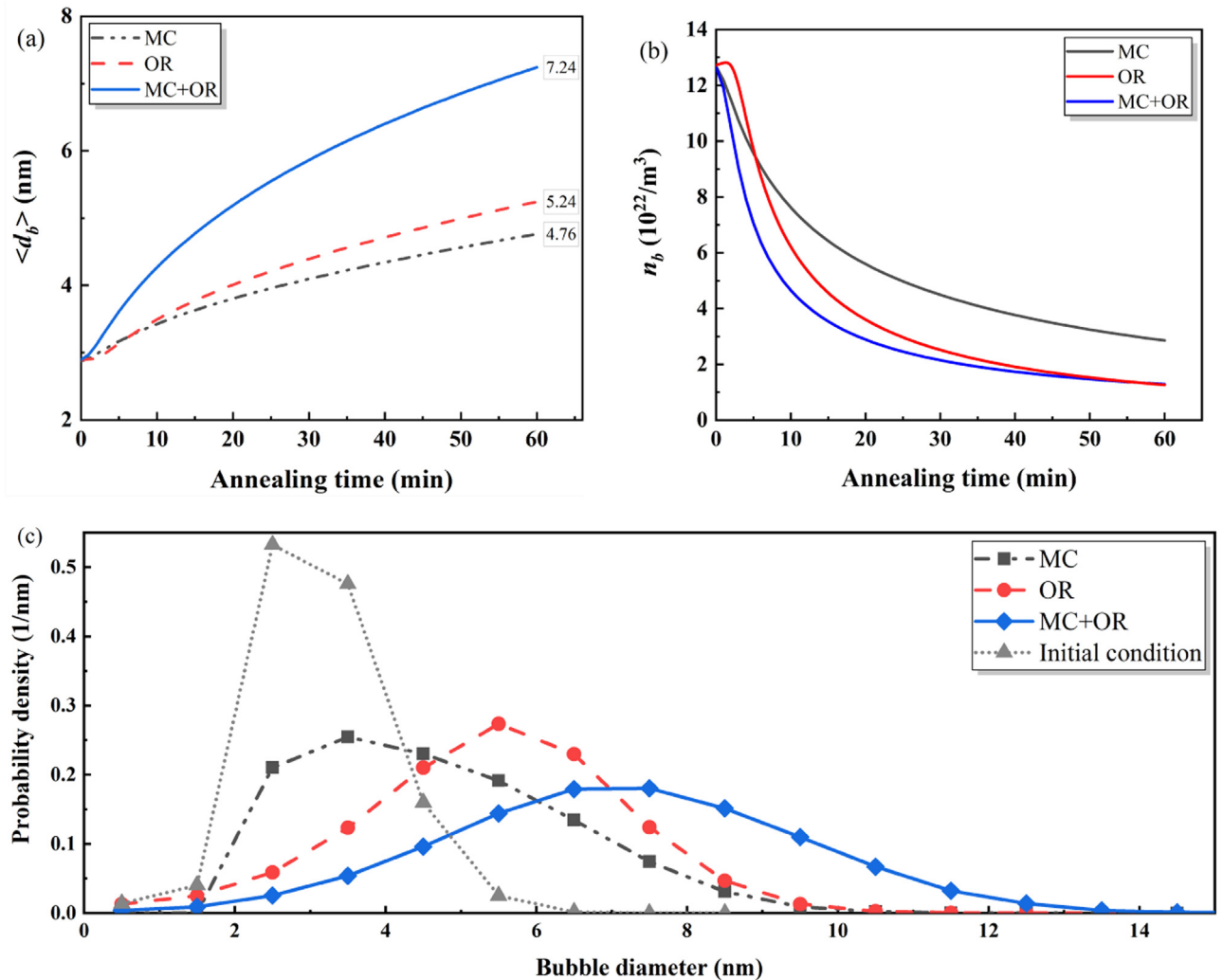


Fig. 8. (a) $\langle d_b \rangle$ and (b) n_b vs. annealing time simulated by PBE at 1073 K when the bubble coarsening is driven by MC, OR, and MC plus OR (MC+OR); (c) The probability density distribution of the final diameter of helium bubbles simulated by PBE at 1073 K when the bubble coarsening driven by MC, OR and MC plus OR (MC+OR). The dotted line is the initial condition for the simulations in this section which is a simulation result of stage III, and the region it covers is called the initial bubble region.

in the enhancement of the coalescence effect and Ostwald ripening effect. It can be seen from Fig. 9 (c) that the probability density of helium bubble size is Gaussian distribution at different temperatures and the variance σ^2 and mean μ of the distributions gradually rise with increasing temperature. The rise of the mean corresponds to the growth of $\langle d_b \rangle$, and the reason for the increase of the variance is mainly the intensification of the Ostwald ripening effect. It can also be concluded from Fig. 9 (a) and (b) that $\langle d_b(t) \rangle$ is gradually proportional to $t^{1/3}$ and $n_b(t)$ is gradually proportional to $t^{-2/3}$, which is consistent with the theoretical analysis of Kiani et al. [46] for the coarsening of helium bubbles driven by the OR mechanism. This indicates that the OR mechanism is the dominant mechanism of the evolution of $\langle d_b \rangle$ and n_b at annealing temperatures greater than or equal to 1073 K.

It has been inferred from Figs. 9 (a) and (b) that the OR mechanism dominates the helium bubble evolution, but the quantitative analysis of its contribution and the variation of its contribution with temperature is still of interest. Since the numerical solution of the population balance equation in Section 3 treats the helium bubble coalescence term separately from the helium bubble continuous growth term, the respective contributions of MC and

OR mechanisms in the evolution of helium bubbles can be calculated by PBE simulation. During the solution for each time step, three phased $\langle d_b \rangle$ can be obtained. These are the initial $\langle d_b \rangle_0$ of helium bubbles $\langle d_b \rangle_0$, the average diameter of helium bubbles after the bubble coalescence $\langle d_b \rangle_1$ obtained by solving Eq. (31), and the average diameter of helium bubbles after the Ostwald ripening mechanism has taken effect $\langle d_b \rangle_2$ obtained by the Lagrangian plus remap approach, and $\langle d_b \rangle_2$ is also the terminal $\langle d_b \rangle$ of the current time step. Then the contribution of MC to the growth of the helium bubble size can be obtained as $\eta_{MC} = \frac{\langle d_b \rangle_1 - \langle d_b \rangle_0}{\langle d_b \rangle_2 - \langle d_b \rangle_0}$, and the contribution of OR can be calculated as $\eta_{OR} = \frac{\langle d_b \rangle_2 - \langle d_b \rangle_1}{\langle d_b \rangle_2 - \langle d_b \rangle_0}$.

Fig. 9 (d) shows the evolution of the contribution ratios of the MC mechanism and the OR mechanism to the growth of $\langle d_b \rangle$ at three annealing temperatures, and it can be summarized from the figure that the contribution ratios of the two mechanisms will reach stable values at a specified temperature (1073 K: 60%OR, 40%MC; 1173 K: 72%OR, 28%MC; 1273 K: 76% OR, 24%MC). And the contribution ratio of the OR mechanism rises with the increasing annealing temperature, indicating that the higher the annealing temperature, the higher the dominance of OR.

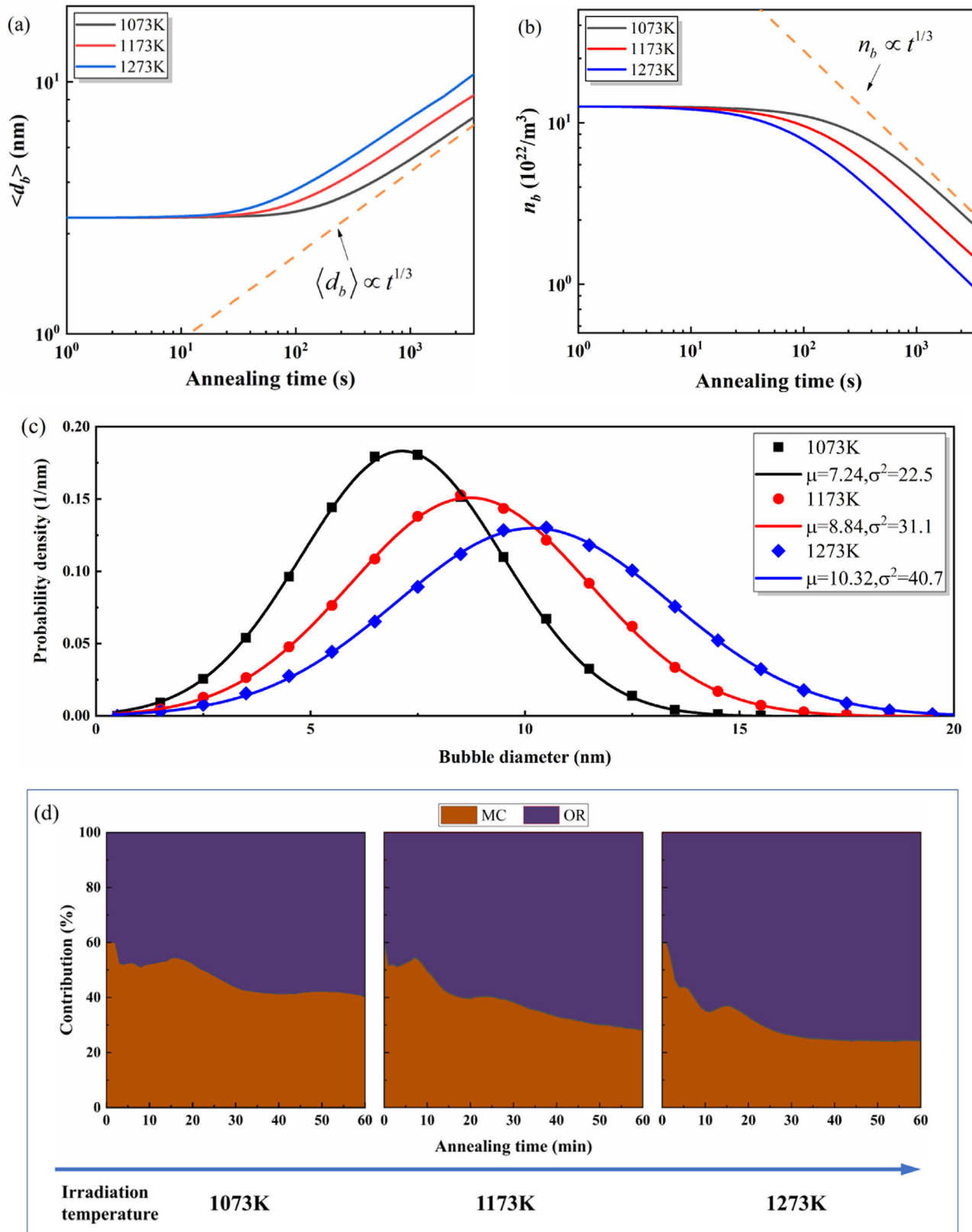


Fig. 9. (a) $\langle d_b \rangle$ and (b) n_b vs. annealing time at 1073 K, 1173 K and 1273 K simulated by PBE; (c) the final probability density distribution of helium bubble diameter at 1073 K, 1173 K and 1273 K simulated by PBE, the scattered points are the simulation results and the solid lines are the Gaussian fit results; (d) the contribution of MC and OR mechanisms to helium bubble diameter growth vs. annealing time at 1073 K, 1173 K and 1273 K.

5. Conclusion

In this paper, a multiscale simulation model of helium bubble evolution is developed by coupling the rate equations and the population balance equation. The model links the nucleation, initial growth and coarsening of helium bubbles. And the model reasonably reproduces the average diameter, density and size distribution of experimentally observed helium bubbles [29,30], and the maximum relative error between the average diameter of helium bubbles simulated by the model and the experimental statistic is less than 10%. In addition, the effects of annealing temperature and time, irradiation energy and flux, and coarsening mechanisms on the evolution of the average size, density and size distribution of the helium bubbles are analyzed using this multiscale model, and the main conclusions are obtained as follows:

- (1) The Ostwald ripening mechanism makes the helium bubbles whose sizes are smaller than the critical dimension release the helium atoms and vacancies, leading to shrinkage and even disappearance of these bubbles. While the helium bubbles become smaller, their coalescence rate and efficiency with large-sized helium bubbles would increase. Therefore, the proportion of small-sized helium bubbles formed by Ostwald ripening can be effectively reduced, and the proportion of large-sized helium bubbles can be increased when the coalescence effect is coupled with the Ostwald ripening, so that the excessive attenuation of helium bubble density can be avoided while the average size of helium bubbles is further increasing.
- (2) Under the condition of high annealing temperature, the Ostwald ripening mechanism dominates the evolution of helium bubbles, and the higher the temperature, the stronger the dominance. And the average diameter of helium bubbles ($d_b(t)$) and helium bubble density $n_b(t)$ are approximated with functions as being proportional to $t^{1/3}$ and $t^{-2/3}$, respectively, which corresponds with the existing theoretical analysis and experiment [46].
- (3) Under the same irradiation flux and different irradiation energy (10kV ~ 100kV), the ratio of the generation rate of helium to the generation rate of vacancy (G_{He}/G_{Vac}) determines the strength of the helium bubble nucleation effect during the nucleation and initial growth period, so the bubble density after helium bubble nucleation is positively correlated with G_{He}/G_{Vac} . However, after the coalescence between bubbles during annealing, the final average diameter of helium bubbles is positively correlated with the generation rate of helium and vacancy.
- (4) Under the same energy and different irradiation flux ($5 \times 10^{12} \sim 5 \times 10^{13}$ ions/cm² · s), the average bubble size and bubble density are positively correlated with the irradiation flux, and the final total volume of helium bubbles is approximately proportional to the irradiation flux.

Declaration of Competing Interest

The authors declare that they have no conflict of interest.

CRediT authorship contribution statement

Qi Li: Conceptualization, Methodology, Software, Validation, Formal analysis, Investigation, Resources, Data curation, Writing – original draft, Writing – review & editing, Visualization, Supervision, Project administration. **Chibin Zhang:** Methodology, Resources, Software, Supervision. **XiaoHui Lin:** Conceptualization, Methodology, Writing – original draft, Writing – review & editing, Supervision. **Chenlong Liu:** Methodology, Resources, Data curation. **Yan Xing:** Project administration, Funding acquisition, Supervision, Writing – review & editing.

Data availability

Data will be made available on request.

Acknowledgment

This work was supported by the National Natural Science Foundation of China (Grant No. 51875104).

Reference

- [1] C.C. Fu, J.D. Torre, F. Willaime, J.L. Bocquet, A. Barbu, Multiscale modelling of defect kinetics in irradiated iron, *Nat. Mater.* 4 (2005) 68–74 t.
- [2] A.W. Robertson, C.S. Allen, Y.A. Wu, K. He, J. Olivier, J. Neethling, A.I. Kirkland, J.H. Warner, Spatial control of defect creation in graphene at the nanoscale, *Nat. Commun.* (2012) 3, doi:[10.1038/ncomms2141](https://doi.org/10.1038/ncomms2141).
- [3] J. Knaster, A. Moeslang, T. Muroga, Materials research for fusion, *Nat. Phys.* 12 (2016) 424–434 a.
- [4] K. Fukumoto, M. Narui, H. Matsui, K. Ito, Y. Yano, Development of irradiation capsules in liquid metal environment in joyo and their application to irradiation creep measurement of vanadium alloys, *J. Nucl. Sci. Technol.* 45 (2008) 171–178, doi:[10.1080/18811248.2008.9711426](https://doi.org/10.1080/18811248.2008.9711426).
- [5] P.D. Edmondson, K.J. Abrams, J.A. Hinks, G. Greaves, C.J. Pawley, I. Hanif, S.E. Donnelly, An *in situ* transmission electron microscopy study of the ion irradiation induced amorphisation of silicon by He and Xe, *Scr. Mater.* 113 (2016) 190–193, doi:[10.1016/j.scriptamat.2015.11.010](https://doi.org/10.1016/j.scriptamat.2015.11.010).
- [6] O. El-Atwani, E. Aydogan, E. Esquivel, M. Efe, Y.Q. Wang, S.A. Maloy, Detailed transmission electron microscopy study on the mechanism of dislocation loop rafting in tungsten, *Acta Mater.* 147 (2018) 277–283, doi:[10.1016/j.actamat.2018.01.003](https://doi.org/10.1016/j.actamat.2018.01.003).
- [7] M.R. Gilbert, J.C. Sublet, Neutron-induced transmutation effects in W and W-alloys in a fusion environment, *Nucl. Fusion* (2011) 51, doi:[10.1088/0029-5515/51/4/043005](https://doi.org/10.1088/0029-5515/51/4/043005).
- [8] J. Gao, E. Gaganidze, B. Kaiser, J. Aktaa, Evolution mechanisms of irradiation-induced helium bubbles, C15 clusters and dislocation loops in ferrite/martensite steels: a cluster dynamics modeling study, *J. Nucl. Mater.* 557 (2021) 153212, doi:[10.1016/j.jnucmat.2021.153212](https://doi.org/10.1016/j.jnucmat.2021.153212).
- [9] C.A. Dennett, K.P. So, A. Kushima, D.L. Buller, K. Hattar, M.P. Short, Detecting self-ion irradiation-induced void swelling in pure copper using transient grating spectroscopy, *Acta Mater.* 145 (2018) 496–503, doi:[10.1016/j.actamat.2017.12.007](https://doi.org/10.1016/j.actamat.2017.12.007).
- [10] L. Wang, T. Hao, B.L. Zhao, T. Zhang, Q.F. Fang, C.S. Liu, X.P. Wang, L. Cao, Evolution behavior of helium bubbles and thermal desorption study in helium-charged tungsten film, *J. Nucl. Mater.* 508 (2018) 107–115 [8], doi:[10.1016/j.jnucmat.2018.05.033](https://doi.org/10.1016/j.jnucmat.2018.05.033).
- [11] J. Chen, P. Jung, T. Rebac, F. Duval, T. Sauvage, Y. De Carlan, M.F. Barthe, Helium effects on creep properties of Fe-14CrWTi ODS steel at 650°C, *J. Nucl. Mater.* 453 (2014) 253–258, doi:[10.1016/j.jnucmat.2014.07.010](https://doi.org/10.1016/j.jnucmat.2014.07.010).
- [12] T. Wei, A. Xu, H. Zhu, M. Ionescu, D. Bhattacharyya, *In situ* micro-compression testing of He²⁺ ion irradiated titanium aluminide, *Nucl. Instrum. Methods Phys. Res. Sect. B Beam Interact. Mater. Atoms* 409 (2017) 288–292, doi:[10.1016/j.nimb.2017.04.042](https://doi.org/10.1016/j.nimb.2017.04.042).
- [13] J.C. Zhang, S. Sun, Z.M. Yang, N. Qiu, Y. Wang, Extended damage range of (Al_{0.3}Cr_{0.2}Fe_{0.2}Ni_{0.3})₃O₄ high entropy oxide films induced by surface irradiation, *Chin. Phys. B* 29 (2020) 0–5, doi:[10.1088/1674-1056/ab8374](https://doi.org/10.1088/1674-1056/ab8374).
- [14] C.S. Kim, R.G. Hobbs, A. Agarwal, Y. Yang, V.R. Manfrinato, M.P. Short, J. Li, K.K. Berggren, Focused-helium-ion-beam blow forming of nanostructures: radiation damage and nanofabrication, *Nanotechnology* (2020) 31, doi:[10.1088/1361-6528/ab4a65](https://doi.org/10.1088/1361-6528/ab4a65).
- [15] G. Hlawacek, *Ion Microscopy*, Springer Handbooks, 2019, doi:[10.1007/978-3-030-00069-1_14](https://doi.org/10.1007/978-3-030-00069-1_14).
- [16] Q. Li, X.H. Lin, C. Zhang, Q. Chen, T. Shao, Y. Xing, Damage profile evolution model based on the Boltzmann transport equation for silicon micromachining with the focused helium ion beam, *Sens. Actuat. A Phys.* 328 (2021), doi:[10.1016/j.sna.2021.112802](https://doi.org/10.1016/j.sna.2021.112802).
- [17] K. Nordlund, Historical review of computer simulation of radiation effects in materials, *J. Nucl. Mater.* 520 (2019) 273–295, doi:[10.1016/j.jnucmat.2019.04.028](https://doi.org/10.1016/j.jnucmat.2019.04.028).
- [18] J.F. Ziegler, M.D. Ziegler, J.P. Biersack, SRIM - the stopping and range of ions in matter (2010), *Nucl. Instrum. Methods Phys. Res. Sect. B Beam Interact. Mater. Atoms* 268 (2010) 1818–1823, doi:[10.1016/j.nimb.2010.02.091](https://doi.org/10.1016/j.nimb.2010.02.091).
- [19] C.S. Deo, M.A. Okuniewski, S.G. Srivilliputhur, S.A. Maloy, M.I. Baskes, M.R. James, J.F. Stubbins, Helium bubble nucleation in bcc iron studied by kinetic Monte Carlo simulations, *J. Nucl. Mater.* 361 (2007) 141–148, doi:[10.1016/j.jnucmat.2006.12.018](https://doi.org/10.1016/j.jnucmat.2006.12.018).
- [20] S. Sharafat, N.M. Ghoniem, Comparison of a microstructure evolution model with experiments on irradiated vanadium, *J. Nucl. Mater.* 283–287 (2000) 789–793, doi:[10.1016/S0022-3115\(00\)00075-1](https://doi.org/10.1016/S0022-3115(00)00075-1).
- [21] E. Gao, N.M. Ghoniem, A coupled rate theory-Monte Carlo model of helium bubble evolution in plasma-facing micro-engineered tungsten, *J. Nucl. Mater.* 509 (2018) 577–590, doi:[10.1016/j.jnucmat.2018.04.051](https://doi.org/10.1016/j.jnucmat.2018.04.051).
- [22] A.M. Ito, A. Takayama, Y. Oda, T. Tamura, R. Kobayashi, T. Hattori, S. Ogata, N. Ohno, S. Kajita, M. Yajima, Y. Noiri, Y. Yoshimoto, S. Saito, S. Takamura,

- T. Murashima, M. Miyamoto, H. Nakamura, Molecular dynamics and Monte Carlo hybrid simulation for fuzzy tungsten nanostructure formation, *Nucl. Fusion* (2015) 55, doi:[10.1088/0029-5515/55/7/073013](https://doi.org/10.1088/0029-5515/55/7/073013).
- [23] S. Sharafat, A. Takahashi, K. Nagasawa, N. Ghoniem, A description of stress driven bubble growth of helium implanted tungsten, *J. Nucl. Mater.* 389 (2009) 203–212, doi:[10.1016/j.jnucmat.2009.02.027](https://doi.org/10.1016/j.jnucmat.2009.02.027).
- [24] A. Takahashi, S. Sharafat, K. Nagasawa, N. Ghoniem, Kinetic Monte Carlo simulation of helium-bubble evolution in ODS steels, *ASTM Spec. Tech. Publ.* 1513 STP (2010) 176–195, doi:[10.1520/stp49009s](https://doi.org/10.1520/stp49009s).
- [25] J. Dérès, M.L. David, K. Alix, C. Hébert, D.T.L. Alexander, L. Pizzagalli, Properties of helium bubbles in covalent systems at the nanoscale: a combined numerical and experimental study, *Phys. Rev. B* 96 (2017) 1–12, doi:[10.1103/PhysRevB.96.014110](https://doi.org/10.1103/PhysRevB.96.014110).
- [26] A. Abhishek, M. Warrier, R. Ganesh, A. Caro, Growth and structural determination of He bubbles in iron/chromium alloys using molecular dynamics simulations, *J. Nucl. Mater.* 472 (2016) 82–88, doi:[10.1016/j.jnucmat.2016.02.001](https://doi.org/10.1016/j.jnucmat.2016.02.001).
- [27] H. Trinkaus, B.N. Singh, Helium accumulation in metals during irradiation – where do we stand? *J. Nucl. Mater.* 323 (2003) 229–242, doi:[10.1016/j.jnucmat.2003.09.001](https://doi.org/10.1016/j.jnucmat.2003.09.001).
- [28] M. Shiea, A. Buffo, M. Vanni, D. Marchisio, Numerical methods for the solution of population balance equations coupled with computational fluid dynamics, *Annu. Rev. Chem. Biomol. Eng.* 11 (2020) 339–366, doi:[10.1146/annurev-chembiomed-092319-075814](https://doi.org/10.1146/annurev-chembiomed-092319-075814).
- [29] Y.P. Li, G. Ran, X.Y. Liu, X. Qiu, Q. Han, W.J. Li, Y.J. Guo, *In-situ* TEM observation of the evolution of helium bubbles in Mo during He⁺ irradiation and post-irradiation annealing, *Chin. Phys. B* (2021) 30, doi:[10.1088/1674-1056/abff48](https://doi.org/10.1088/1674-1056/abff48).
- [30] Y. Chen, Y. Li, G. Ran, L. Wu, C. Ye, Q. Han, H. Wang, H. Du, *In-situ* TEM observation of the evolution of dislocation loops and helium bubbles in a pre helium irradiated FeCrAl alloy during annealing, *Prog. Nucl. Energy* (2020) 129, doi:[10.1016/j.pnucene.2020.103502](https://doi.org/10.1016/j.pnucene.2020.103502).
- [31] A.A.F. Tavassoli, Present limits and improvements of structural materials for fusion reactors - a review, *J. Nucl. Mater.* 302 (2002) 73–88, doi:[10.1016/S0022-3115\(02\)00794-8](https://doi.org/10.1016/S0022-3115(02)00794-8).
- [32] B.A. Pint, K.A. Terrani, Y. Yamamoto, L.L. Snead, Material selection for accident tolerant fuel cladding, *Metall. Mater. Trans. E* 2 (2015) 190–196, doi:[10.1007/s40553-015-0056-7](https://doi.org/10.1007/s40553-015-0056-7).
- [33] C. Zhenhua, J. Xiangyang, W. Yun, Z. Duosan, The constitution of multicomponent quasi-crystalline alloys, *J. Mater. Sci. Lett.* 11 (1992) 1493–1495, doi:[10.1007/BF00729269](https://doi.org/10.1007/BF00729269).
- [34] M. Kiani, F. Samavat, J. O'Connor, Phason mechanism for diffusion in quasicrystalline structures, *Solid State Commun.* 321 (2020) 114017, doi:[10.1016/j.ssc.2020.114017](https://doi.org/10.1016/j.ssc.2020.114017).
- [35] T. Zumkley, H. Mehrer, K. Freitag, Diffusion of Mn 54 and Fe 59 in icosahedral Al-Pd-Mn single quasicrystals, *Phys. Rev. B Condens. Matter Mater. Phys.* 54 (1996) R6815–R6818, doi:[10.1103/PhysRevB.54.R6815](https://doi.org/10.1103/PhysRevB.54.R6815).
- [36] N.M. Ghoniem, J.N. Alhajji, D. Kaletta, The effect of helium clustering on its transport to grain boundaries, *J. Nucl. Mater.* 136 (1985) 192–206, doi:[10.1016/S0022-3115\(85\)90007-8](https://doi.org/10.1016/S0022-3115(85)90007-8).
- [37] J.P. Barbour, F.M. Charbonnier, W.W. Dolan, W.P. Dyke, E.E. Martin, J.K. Trolan, Determination of the surface tension and surface migration constants for tungsten, *Phys. Rev.* 117 (1960) 1452–1459, doi:[10.1103/PhysRev.117.1452](https://doi.org/10.1103/PhysRev.117.1452).
- [38] G.W. Egeland, J.A. Valdez, S.A. Maloy, K.J. McClellan, K.E. Sickafus, G.M. Bond, Heavy-ion irradiation defect accumulation in ZrN characterized by TEM, GIXRD, nanoindentation, and helium desorption, *J. Nucl. Mater.* 435 (2013) 77–87, doi:[10.1016/j.jnucmat.2012.12.025](https://doi.org/10.1016/j.jnucmat.2012.12.025).
- [39] P.J. Goodhew, S.K. Tyler, Helium bubble behaviour in bcc metals below 0.65 Tm, *Proc. R. Soc. London. A Math. Phys. Sci.* 377 (1981) 151–184, doi:[10.1098/rspa.1981.0120](https://doi.org/10.1098/rspa.1981.0120).
- [40] F. Nichols, Kinetics of diffusional motion of pores in solids: a review, *J. Nucl. Mater.* 30 (1–2) (1969) 143–165, doi:[10.1016/0022-3115\(69\)90176-7](https://doi.org/10.1016/0022-3115(69)90176-7).
- [41] K. Ono, S. Furuno, S. Kanamitu, K. Hojou, *In-situ* observation of Brownian motion of helium bubbles along grain boundaries in aluminium, *Philos. Mag. Lett.* 75 (1997) 59–64, doi:[10.1080/095008397179750](https://doi.org/10.1080/095008397179750).
- [42] K. Ono, K. Arakawa, K. Hojou, M. Oohasi, R.C. Birtcher, S.E. Donnelly, Quantitative study of Brownian motion of helium bubbles in fcc metals, *J. Electron Microsc. (Tokyo)* 51 (2002) 245–251, doi:[10.1093/jmicro/51.supplement.s245](https://doi.org/10.1093/jmicro/51.supplement.s245).
- [43] A. Einstein, Theoretische Bemerkungen Über die Brownsche Bewegung, *Zeitschrift für Elektrochemie und Angewandte Physikalische Chemie* 13 (1907) 41–42, doi:[10.1002/bbpc.19070130602](https://doi.org/10.1002/bbpc.19070130602).
- [44] J.H. Evans, Breakaway bubble growth during the annealing of helium bubbles in metals, *J. Nucl. Mater.* 334 (2004) 40–46, doi:[10.1016/j.jnucmat.2004.04.349](https://doi.org/10.1016/j.jnucmat.2004.04.349).
- [45] Z. Borka, H.A. Jakobsen, Evaluation of breakage and coalescence kernels for vertical bubbly flows using a combined multifluid-population balance model solved by least squares method, *Proc. Eng.* 42 (2012) 623–633, doi:[10.1016/j.proeng.2012.07.455](https://doi.org/10.1016/j.proeng.2012.07.455).
- [46] A.M. Ovcharenko, I.I. Chernov, On the theory of bubble coarsening in metals, *J. Nucl. Mater.* 528 (2020) 151824, doi:[10.1016/j.jnucmat.2019.151824](https://doi.org/10.1016/j.jnucmat.2019.151824).
- [47] W. Dai, R. Nassar, Compact ADI method for solving parabolic differential equations, *Numer. Methods Partial Differ. Equ.* 18 (2002) 129–142, doi:[10.1002/num.1037](https://doi.org/10.1002/num.1037).
- [48] S.K. Lele, Compact finite difference schemes with spectral-like resolution, *J. Comput. Phys.* 103 (1992) 16–42, doi:[10.1016/0021-9991\(92\)90324-R](https://doi.org/10.1016/0021-9991(92)90324-R).
- [49] J. Kumar, M. Peglow, G. Warnecke, S. Heinrich, An efficient numerical technique for solving population balance equation involving aggregation, breakage, growth and nucleation, *Powder Technol.* 182 (2008) 81–104, doi:[10.1016/j.powtec.2007.05.028](https://doi.org/10.1016/j.powtec.2007.05.028).
- [50] J.L. Cao, W.T. Geng, Migration of helium-pair in metals, *J. Nucl. Mater.* 478 (2016) 13–25, doi:[10.1016/j.jnucmat.2016.05.030](https://doi.org/10.1016/j.jnucmat.2016.05.030).
- [51] P.W. Ma, S.L. Dudarev, Symmetry-broken self-interstitial defects in chromium, molybdenum, and tungsten, *Phys. Rev. Mater.* 3 (2019), doi:[10.1103/PhysRevMaterials.3.043606](https://doi.org/10.1103/PhysRevMaterials.3.043606).
- [52] C. Jiang, Y. Zhang, L.K. Aagesen, A.M. Jokisaari, C. Sun, J. Gan, Noble gas bubbles in bcc metals: *ab initio*-based theory and kinetic Monte Carlo modeling, *Acta Mater.* 213 (2021) 116961, doi:[10.1016/j.actamat.2021.116961](https://doi.org/10.1016/j.actamat.2021.116961).
- [53] D. Nguyen-Manh, A.P. Horsfield, S.L. Dudarev, Self-interstitial atom defects in bcc transition metals: group-specific trends, *Phys. Rev. B Condens. Matter Mater. Phys.* 73 (2006) 4–7, doi:[10.1103/PhysRevB.73.020101](https://doi.org/10.1103/PhysRevB.73.020101).
- [54] L.F. Wang, X. Shu, G.H. Lu, Comparison of two tungsten–helium interatomic potentials, *J. Mater. Res.* 30 (2015) 1464–1472, doi:[10.1557/jmr.2014.407](https://doi.org/10.1557/jmr.2014.407).
- [55] C.S. Becquart, C. Domain, U. Sarkar, A. Debacker, M. Hou, Microstructural evolution of irradiated tungsten: *ab initio* parameterisation of an OKMC model, *J. Nucl. Mater.* 403 (2010) 75–88, doi:[10.1016/j.jnucmat.2010.06.003](https://doi.org/10.1016/j.jnucmat.2010.06.003).
- [56] G.K. Williamson, R.E. Smallman III, Dislocation densities in some annealed and cold-worked metals from measurements on the X-ray Debye–Scherrer spectrum, *Philos. Mag.* 1 (1956) 34–46, doi:[10.1080/147864356082338074](https://doi.org/10.1080/147864356082338074).
- [57] C.J. Ortiz, M.J. Caturla, C.C. Fu, F. Willaime, He diffusion in irradiated α -Fe: an *ab-initio*-based rate theory model, *Phys. Rev. B Condens. Matter Mater. Phys.* 75 (2007) 1–4, doi:[10.1103/PhysRevB.75.100102](https://doi.org/10.1103/PhysRevB.75.100102).
- [58] H. Trinkaus, The effect of internal pressure on the coarsening of inert gas bubbles in metals, *Scr. Metall.* 23 (1989) 1773–1778, doi:[10.1016/0036-9748\(89\)90359-1](https://doi.org/10.1016/0036-9748(89)90359-1).